

Thermoelectric Generation Based on Spin Seebeck Effects

The study of combined heat and spin flow, called spin caloritronics, may be used to develop more efficient thermoelectric conversion. Device structures using the most widely considered effect, the longitudinal spin Seebeck effect, differ significantly from conventional devices due to the orthogonality of the thermal gradient and resulting charge current, giving different strategies for applications.

By KEN-ICHI UCHIDA, HIROTO ADACHI, TAKASHI KIKKAWA, AKIHIRO KIRIHARA, MASAHICO ISHIDA, SHINICHI YOROZU, SADAMICHI MAEKAWA, AND EIJI SAITOH

ABSTRACT | The spin Seebeck effect (SSE) refers to the generation of a spin current as a result of a temperature gradient in magnetic materials including insulators. The SSE is applicable to thermoelectric generation because the thermally generated spin current can be converted into a charge current via spin-orbit interaction in conductive materials adjacent to the magnets. The insulator-based SSE device exhibits unconventional characteristics potentially useful for thermoelectric applications, such as simple structure, device-design flexibility, and convenient scaling capability. In this article, we review recent studies on the SSE from the viewpoint of thermoelectric applications. Firstly, we introduce the

thermoelectric generation process and measurement configuration of the SSE, followed by showing fundamental characteristics of the SSE device. Secondly, a theory of the thermoelectric conversion efficiency of the SSE device is presented, which clarifies the difference between the SSE and conventional thermoelectric effects and the efficiency limit of the SSE device. Finally, we show preliminary demonstrations of the SSE in various device structures for future thermoelectric applications and discuss prospects of the SSE-based thermoelectric technologies.

KEYWORDS | Anomalous Nernst effect; inverse spin Hall effect; magnetic material; spin current; spin Seebeck effect; spintronics; thermoelectric generation; thin film

Manuscript received August 29, 2015; revised December 23, 2015; accepted February 17, 2016. Date of publication April 14, 2016; date of current version September 16, 2016. This work was supported by PRESTO "Phase Interfaces for Highly Efficient Energy Utilization" from JST, Japan, Grant-in-Aid for Scientific Research (A) (15H02012), Grant-in-Aid for Challenging Exploratory Research (26600067), Grant-in-Aid for Scientific Research on Innovative Area, "Nano Spin Conversion Science" (26103005) from MEXT, Japan, and NEC Corporation. T.K. is supported by JSPS through a research fellowship for young scientists (15J08026).

K. Uchida is with the Institute for Materials Research, Tohoku University, Sendai 980-8577, Japan, and also with the PRESTO, Japan Science and Technology Agency, Saitama 332-0012, Japan (e-mail: kuchida@imr.tohoku.ac.jp).

H. Adachi and **S. Maekawa** are with the Advanced Science Research Center, Japan Atomic Energy Agency, Tokai, 319-1195, Japan, and also with the Spin Quantum Rectification Project, ERATO, Japan Science and Technology Agency, Sendai 980-8577, Japan.

T. Kikkawa is with the Institute for Materials Research, Tohoku University, Sendai 980-8577, Japan, and also with the WPI Advanced Institute for Materials Research, Tohoku University, Sendai 980-8577, Japan.

A. Kirihara, **M. Ishida**, and **S. Yorozu** are with the Spin Quantum Rectification Project, ERATO, Japan Science and Technology Agency, Sendai 980-8577, Japan, and also with the Smart Energy Research Laboratories, NEC Corporation, Tsukuba 305-8501, Japan.

E. Saitoh is with the Institute for Materials Research, Tohoku University, Sendai 980-8577, Japan, with the Advanced Science Research Center, Japan Atomic Energy Agency, Tokai 319-1195, Japan, with the Spin Quantum Rectification Project, ERATO, Japan Science and Technology Agency, Sendai 980-8577, Japan and with the WPI Advanced Institute for Materials Research, Tohoku University, Sendai 980-8577, Japan.

Digital Object Identifier: 10.1109/JPROC.2016.2535167

I. INTRODUCTION

Heat is an omnipresent and abundant source of energy, and thus the efficient utilization of thermal energy, such as waste heat recovery and solar heat power generation, is indispensable for the realization of future sustainable society. Thermoelectric generation is one of the promising technologies for making effective use of heat since it enables direct conversion from thermal energy to electrical power [1]–[3]. As thermoelectric devices consist of solid-state materials and have no moving parts, they are silent, reliable, and scalable. Most of the prevalent thermoelectric generation technologies are based on the Seebeck effect, discovered by T. J. Seebeck in 1821 [4], [5]. Although a variety of thermoelectric effects were found to appear in electric conductors subjected to temperature gradients after the discovery of the Seebeck effect [6], the earliest thermoelectric phenomenon is still the key

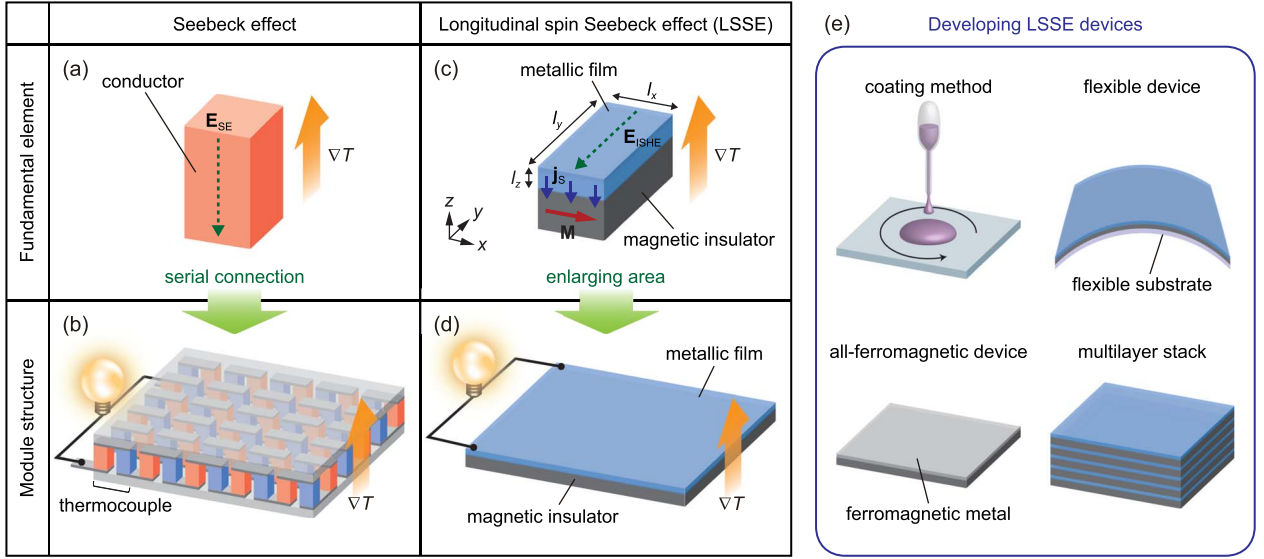


Fig. 1. (a), (b) Schematic illustrations of the fundamental element and module structure of the thermoelectric device based on the Seebeck effect. (c), (d) Schematic illustrations of the fundamental element and module structure of the thermoelectric device based on the longitudinal spin Seebeck effect (LSSE). ∇T , $E_{SE(ISH)}$, M , and j_s denote the temperature gradient, electric field generated by the Seebeck effect [inverse spin Hall effect (ISHE)], magnetization vector, and spatial direction of the thermally generated spin current, respectively. $l_{x(y)}$ is the length of the metallic film of the LSSE device along the x (y) direction and l_z is the thickness of the metallic film. (e) Schematic illustrations of the LSSE-device structures being developed for future thermoelectric applications.

player in the thermoelectric technology because of its relatively-high output power and versatility.

The Seebeck effect refers to the generation of an electric field E_{SE} as a result of a temperature gradient ∇T in a conductor, where the direction of E_{SE} is parallel to that of ∇T [see Fig. 1(a)]. The thermopower induced by the Seebeck effect is represented by the Seebeck coefficient: $\alpha \equiv E_{SE}/\nabla T$, which is equal to the ratio of the generated electric voltage to the applied temperature difference owing to the collinear orientation of E_{SE} and ∇T . A thermoelectric module based on the Seebeck effect usually consists of a number of Π -structured thermocouples, i.e., junctions of two materials with different Seebeck coefficients; the thermocouples are serially connected to enhance the thermoelectric output [see Fig. 1(b)]. The output voltage of the thermoelectric module can be enhanced in proportion to the number of the thermocouple elements, although such cascaded structure requires costly fabrication processes.

The efficiency of the thermoelectric generation based on the Seebeck effect is characterized by the dimensionless figure of merit $Z_{SE}T$, defined as

$$Z_{SE}T = \frac{\alpha^2}{\kappa\rho} T \quad (1)$$

where κ , ρ , and T are the thermal conductivity, electrical resistivity, and absolute temperature of thermoelectric materials [1]. The factor α^2/ρ is known as a thermoelectric power factor. The efficiency of the Seebeck device for electricity generation is defined as $\eta = (\text{energy provided to a load})/(\text{heat energy absorbed at the hot end of the device})$,

which is a function of internal and load resistances. The optimized efficiency η_{SE}^* of the Seebeck device is then given as a function of the figure of merit as follows:

$$\eta_{SE}^* = \frac{\Delta T}{T_h} \frac{\sqrt{1 + Z_{SE}\bar{T}} - 1}{\sqrt{1 + Z_{SE}\bar{T}} + \frac{T_c}{T_h}} \quad (2)$$

where $\Delta T = T_h - T_c$ is the temperature difference between the hot and cold ends of the device, $T_{h(c)}$ is the temperature at the hot (cold) end, and \bar{T} is the average temperature between the hot and cold ends [4], [5]. Importantly, η_{SE}^* monotonically increases with increasing $Z_{SE}\bar{T}$; η_{SE}^* goes to the Carnot efficiency $\eta_C = \Delta T/T_h$ in the limit of $Z_{SE}\bar{T} \rightarrow \infty$. Therefore, many efforts in thermoelectric research are dedicated to improve the figure of merit of thermoelectric materials.

Equations (1) and (2) mean that materials having a large Seebeck coefficient, low thermal conductivity, and low electrical resistivity are necessary for improving the thermoelectric conversion efficiency. Importantly, low κ and ρ values make it possible to suppress the energy loss due to heat conduction and Joule dissipation, respectively. However, in isotropic metals, the Wiedemann-Franz law ($\kappa_e\rho = L_e T$ with the electronic Lorenz number L_e) limits this improvement when κ is dominated by the electronic thermal conductivity κ_e . A conventional way to overcome this limitation is to use thermoelectric semiconductors, where the thermal conductance is usually dominated by phonons while the electrical conductance is determined by charge carriers, and thus κ and ρ are separated according

to the kind of the carriers [1]. Recently, to improve the figure of merit of thermoelectric materials by reducing phonon thermal conductivity without affecting electrical conductivity, not only exploration of new materials [7], [8] but also nanotechnology-based phonon engineering [9]–[17] have been conducted. Furthermore, research on the thermoelectric properties of anisotropic materials has attracted increasing attention recently [7], [8], [18]–[22]; since the Wiedemann–Franz law is violated in anisotropic materials, they are also useful for optimizing heat and charge conduction separately.

Nearly 200 years after the discovery of the Seebeck effect, a novel thermoelectric generation principle was discovered in the field of spintronics [23]–[25]. This novel principle can be said as a spin counterpart of the Seebeck effect: “spin Seebeck effect” (SSE) [26]. The SSE refers to the generation of a spin current, a flow of spin angular momentum [27], [28], as a result of a temperature gradient in a magnetic material. The SSE is applicable to the construction of thermoelectric generators because the spin current generated by the SSE can be converted into a charge current via the spin-orbit interaction, or the inverse spin Hall effect (ISHE) [29]–[34], in a conductive thin film (mostly, a paramagnetic metal film) adjacent to the magnetic material (see Section II for details). Here, the direction of the electric field induced by the ISHE E_{ISHE} in the conductive film is perpendicular to that of ∇T in the magnetic material [see Fig. 1(c)], a configuration different from the conventional Seebeck effect. Since the SSE appears not only in ferromagnetic metals [26], [35]–[38] and semiconductors [39], [40] but also in magnetic (mostly, ferrimagnetic) insulators [41], [42], it enables the conversion of heat energy in insulators into electrical energy in adjacent conductors [43], [44], which was impossible if only conventional thermoelectric technologies were used. The thermoelectric technology based on the SSE is still in an early phase of its development, and the efficiency is very small at the present stage. However, as reviewed in this article, the SSE exhibits various unconventional features suitable for thermoelectric applications.

In this review, we focus on the so-called longitudinal SSE (LSSE) [42], [44] in metallic film/magnetic insulator junction systems, depicted in Fig. 1(c). After the first report on the SSE [26], this phenomenon has been measured mainly in two different device structures, i.e., the longitudinal and transverse configurations [45], where spin currents parallel and perpendicular to ∇T are measured, respectively. The longitudinal configuration has been used in most of the recent SSE studies because the insulator-based LSSE systems are useful for the exclusive detection of spin-current-induced signals and suitable for thermoelectric applications owing to its simple and versatile structure. The first observation of the LSSE was reported in 2010 by using a junction system comprising a paramagnetic metal Pt and a ferrimagnetic insulator $\text{Y}_3\text{Fe}_5\text{O}_{12}$ (YIG)

[42]. The Pt/YIG junction system is now recognized as a model system for studying SSE physics, since Pt and YIG enable efficient spin-charge conversion and pure detection of spin-current effects, respectively. Since this demonstration, the LSSE has been observed in various combinations of magnetic insulators and conductive films [42]–[110], as shown in Fig. 2. In contrast, in the transverse configuration, the SSE measurements may be disturbed by thermal conductivity mismatch [111], [112] between a film and a substrate that induces parasitic LSSE [113] or anomalous Nernst effect (ANE) [6], [114]–[121], requiring careful thermal design of the sample and measurement systems. In the transverse SSE measurements using conductive ferromagnets, a planar Nernst effect (PNE) [6], [122]–[125] may also arise. In the past several years, various thermoelectric measurements have been performed in the transverse configuration [111]–[113], [122]–[125], and the quantitative separation of the transverse SSE from the parasitic ANE and PNE has been reported in a ferromagnetic metal [38]. In addition to the longitudinal and transverse configurations, a nonlocal geometry has also been used recently to investigate the length scale of the SSE [126]–[129].

The LSSE in insulators allows a new approach to improve the thermoelectric figure of merit. In the insulator-based LSSE device, the heat and charge currents flow in different parts of the device: κ is the thermal conductivity of the magnetic insulator and ρ is the electrical resistivity of the adjacent metal, such that κ and ρ in the LSSE device are segregated according to the part of the device elements [44]. Therefore, the denominator of the figure of merit, $\kappa\rho$, of the LSSE device is free from the Wiedemann–Franz law, and allowed to be optimized if one selects the combination of a magnetic insulator with low thermal conductivity and a metallic film with low electrical resistivity. This is one of the unique characteristics of the LSSE device, although, in addition to the $\kappa\rho$ factor, the LSSE thermopower itself must be improved. Importantly, in fact, the relation between the figure of merit and the thermoelectric conversion efficiency of the LSSE device should be different from that of the conventional Seebeck device due to the different device configurations and driving principles [130]–[132]. One of the purposes of this review article is to formulate the thermoelectric figure of merit and conversion efficiency of the LSSE device, and to clarify the upper limit of the efficiency.

The advantages of the LSSE device include not only the device-design flexibility, discussed above, but also the following characteristics. The LSSE device has convenient scaling capability, where the thermoelectric output increases simply by extending the device area because the total amount of the thermally generated spin currents increases as the device becomes larger [43]. Here, the electric field induced by the ISHE at each point of the LSSE device is integrated into the output LSSE voltage: $V_{\text{SSE}} = E_{\text{ISHE}}l$, where E_{ISHE} is the magnitude of E_{ISHE} and

Conductive film Magnetic insulator	Simple metal											Alloy				Bilayer metal					Oxide	
	Pt	Au	Ir	Pd	Ni*	W	Ta	Mo	Nb	Cr	Ti	NiFe*	FePt*	IrMn	AuCu	Pt /Cu	Pt /Au	Pt /FeCu*	Pt /Ti	CoFeB* /Ti	Co* /Cu	IrO ₂
	positive θ_{SH}					negative θ_{SH}																
Garnet ferrite $Y_3Fe_5O_{12}$ (YIG) $Y_{3-x}R_xFe_{5-y}M_yO_{12}$ $\left[\begin{array}{l} R = Ca, Nd, Gd, Bi \\ M = Al, Mn, Ga, V, In, Zr \end{array} \right]$ $Gd_3Fe_5O_{12}$ $Gd_3Ga_5O_{12}$ (paramagnetic)	<div>Ref. No. 42 50,51 76,103 64 64,75 49 91 55,84 44 44 44 44 44 44 44 Fig. 12 of this article 102 86</div>											56,58,61 96 63 108				51,95 57,59 80 86 87 92						
Spinel ferrite $(Mn,Zn)Fe_2O_4$ Fe_3O_4 $NiFe_2O_4$ $Co_xFe_{3-x}O_4$ ($x = 0.25, 0.75, 1$) $CoCr_2O_4$ (multiferroic) $Ni_{0.2}Zn_{0.3}Fe_{2.5}O_4$	46 54,100 53 85,107 99 106 82 106															70,82 70						
Hexagonal ferrite $BaFe_{12}O_{19}$ $Ba_{0.5}Sr_{1.5}Zn_2Fe_{12}O_{22}$ (multiferroic)	77 110																					
Perovskite La_2NiMnO_6 $La_{0.67}Sr_{0.33}MnO_3$ $DyScO_3$ (paramagnetic)	78 86 86																				89 89	
Corundum Cr_2O_3 (antiferromagnetic)	104																					
Rutile MnF_2 (antiferromagnetic)	105 105															105						

Fig. 2. Combination of magnetic insulators and conductive films used for the observation of the LSSE. The solid circles show the material combinations in which the LSSE have been observed, where the red (blue) circles represent the fact that the sign of the observed LSSE voltage is the same as (opposite to) that in the Pt/YIG systems. The color of the circle showing the Pt/Gd₃Fe₅O₁₂ system is black, since the LSSE in this system exhibits sign reversals as a function of temperature. The numbers near the circles correspond to the reference numbers. The asterisks in the list of the conductive films represent ferromagnetic metals, which enable the hybrid thermoelectric generation based on the LSSE and anomalous Nernst effect (ANE). Typical values for the spin diffusion lengths and spin Hall angles of the conductive materials are summarized in the review on the spin Hall effects [34].

l_y is the length of the metallic layer along the y direction [Fig. 1(c)]. Since the internal resistance of the metallic layer of the LSSE device is $R_{\text{metal}} = \rho l_y / l_x l_z$ with l_x and l_z respectively being the length along the x direction and thickness of the metallic film, the maximum extractable electrical power P_{max} is proportional to the area of the LSSE device: $P_{\text{max}} \propto V_{\text{SSE}}^2 / R_{\text{metal}} \propto l_x l_y$ [see Section III-C]. Such a straightforward scaling law makes it possible to enhance the thermoelectric output simply by enlarging the device area [see Fig. 1(d)]. To exploit the above characteristics of the LSSE device, versatile and low-cost fabrication methods have been developed, such as coating [43] and plating [106] technologies [see Fig. 1(e)]. These methods enable the implementation of simple-structure, large-area, and even flexible LSSE devices onto various heat sources, as shown in Section V-A and B.

The thermoelectric generation based on the LSSE involves the following three factors:

- 1) heat-current/spin-current conversion efficiency in magnetic materials;
- 2) spin-angular-momentum transfer efficiency across metal/insulator interfaces, characterized by the spin mixing conductance [133]–[136];
- 3) spin-current/charge-current conversion efficiency in metallic films, characterized by the spin Hall angle [34], [137].

A direct approach to enhance the performance of the spin-current-driven thermoelectric generation is to improve the LSSE itself [the factor 1)], which realizes efficient thermal spin-current generation [see Section V-D]. In addition to this approach, the improvement of the spin mixing conductance [the factor 2)] and the spin Hall angle [the factor 3)]

are also essential. For example, to realize the efficient spin-angular-momentum transfer across the metal/insulator interface, the improvement of crystal quality and interface condition of the LSSE device by annealing has been conducted [69], [138], [139]. The spin mixing conductance can also be enhanced by inserting an ultrathin ferromagnetic interlayer between a paramagnetic metal and a ferrimagnetic insulator owing to the increase of magnetic moment density at the interface [80], [134]. To realize the efficient spin-charge conversion, the ISHE has been measured in various metals [44], [140]–[142], alloys [56], [58], [61], [63], [70], [96], [108], [143]–[145], semiconductors [146]–[149], oxides [89], [92], [150], [151], and organic materials [152], [153]. The spin mixing conductance and spin Hall angle can be estimated by means of various techniques, such as micro-wave-induced spin pumping [29], [30], [61], [63], [141], [142], [145]–[150], [152]–[157], spin Hall magnetoresistance [158]–[162], and nonlocal methods [31], [33], [140], [143]–[145], [151], [163]–[165], where these phenomena can be measured by applying microwaves or charge currents to similar paramagnet/ferromagnet junction systems instead of temperature gradients. Therefore, not only the LSSE experiments but also these techniques are necessary for optimizing the LSSE devices. Although the conventional LSSE experiments have mainly been performed using paramagnetic metal/ferrimagnetic insulator junction systems, all-ferromagnetic devices [56], [58], [61], [96], i.e., ferromagnetic metal/ferrimagnetic (or ferromagnetic) insulator junction systems, and alternately-stacked metal/insulator multilayer films [100] have recently been recognized as useful tools for improving the thermoelectric performance of the LSSE devices, as shown in Section V-C and D.

In this article, we review recent studies on the LSSE from the viewpoint of thermoelectric applications. This article is organized as follows. We start with an explanation of the thermoelectric generation process and measurement configuration of the LSSE in Section II, followed by experimental demonstrations of the basic characteristics of the LSSE devices in Section III. In Section IV, we formulate the thermoelectric figure of merit and conversion efficiency of the LSSE devices and compare the results with those for conventional thermoelectric devices. In Section V, we show preliminary demonstrations for future thermoelectric applications of the LSSE devices, where we focus on the device structures depicted in Fig. 1(e). The last Section VI is devoted to the conclusions and prospects.

II. THERMOELECTRIC GENERATION PROCESS AND MEASUREMENT CONFIGURATION

Fig. 3(a) shows a schematic illustration of the standard configuration used for the LSSE measurements. The basic structure of the LSSE device consists of a metallic

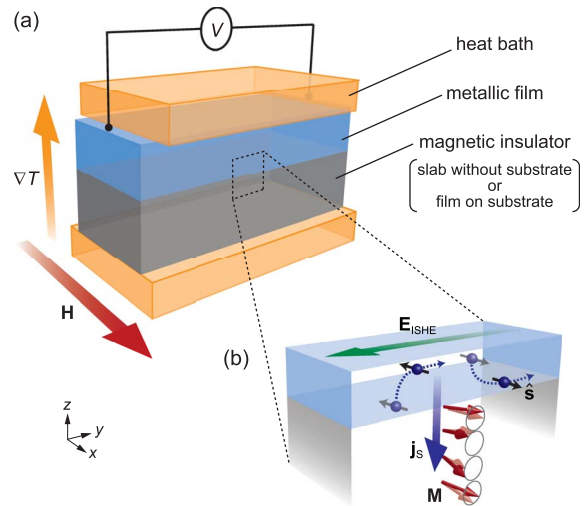


Fig. 3. (a) Schematic illustration of the typical experimental configuration for measuring the LSSE in a junction system comprising a metallic film and a magnetic insulator. ∇T is applied across the metal/insulator interface by sandwiching the LSSE device between two heat baths with different temperatures. When a soft magnetic insulator is used, an external magnetic field H is applied to align the magnetization of the insulator along the x direction. (b) A schematic illustration of the ISHE induced by the LSSE. \hat{s} denotes the unit vector along the electron-spin polarization ($\parallel M$) in the metallic film.

film formed on a magnetic insulator. Here, the magnetic insulator is a slab without a substrate or a film formed on a substrate, while the metallic layer must be a thin film as explained later. In the metal/insulator junction in the longitudinal configuration, the temperature gradient, ∇T , is applied perpendicular to the metal/insulator interface (along the z direction) and the spatial direction of the spin current induced by the LSSE is parallel to the ∇T direction [42]. The LSSE is usually measured with applying an external magnetic field to align the magnetization of the magnetic insulator along the x direction [see Fig. 3(a)]. However, the external magnetic field is not indispensable for the LSSE-based thermoelectric generation if the device comprises a hard-magnetic material [77], [85]. Under this condition, a DC electric voltage difference V between the ends of the metallic film of the LSSE device is measured.

To apply the temperature gradient in the direction perpendicular to the metal/insulator interface, the LSSE device is usually sandwiched between two heat baths which are stabilized at different temperatures [see Fig. 3(a)] [42], [44]. By heating or cooling the heat baths, one can apply a reversible temperature gradient to the LSSE device since its top and bottom surfaces are directly connected to the heat bath [45]. Owing to this high temperature controllability, the setup depicted in Fig. 3(a) is mostly used in the LSSE measurements; all the

experiments shown in this article were performed in this setup. In contrast, the temperature gradient can be applied to the LSSE device also by using Joule heating in an on-chip heater [70], [75], [76], [82], laser heating [47], [48], [57], [66], [67], and microwave heating [52], [68]. Although these methods enable the measurements of the LSSE without using the specialized temperature-gradient generators, it is difficult to determine the temperature distributions; the methods are sometimes combined with numerical simulations [48], [57], [67], [68], [82].

The thermoelectric generation mechanism of the LSSE device is summarized as follows. The driving force of the LSSE is nonequilibrium dynamics of magnons, collective excitations of localized magnetic moments, in the magnetic insulator driven by the temperature gradient [166]–[182], since the LSSE appears even when a conduction electrons' contribution is completely frozen out. This nonequilibrium magnon dynamics in the magnetic insulator can interact with conduction-electron spins in the attached metal and transfer the spin angular momentum across at the metal/insulator interface via the interface s-d exchange interaction, which is described in terms of the spin mixing conductance [133]–[136]. This spin-angular-momentum transfer induces a conduction-electron spin current in the metallic film. This spin current is converted into the electric field, \mathbf{E}_{ISHE} , by the aforementioned ISHE in the metallic layer if the spin-orbit interaction of the metal is strong [Fig. 3(b)]. When the magnetization \mathbf{M} of the magnetic insulator is aligned along the x direction, \mathbf{E}_{ISHE} is generated in the metallic film along the y direction according to the relation [27]

$$\mathbf{E}_{\text{ISHE}} = (\theta_{\text{SH}}\rho)\hat{\mathbf{s}} \times \mathbf{j}_{\text{S}} \quad (3)$$

where θ_{SH} , $\hat{\mathbf{s}}$, and \mathbf{j}_{S} are the spin Hall angle, unit vector along the electron-spin polarization ($\|\mathbf{M}\|$) in the metallic layer, and spatial direction of the spin current (with the magnitude of spin current density j_{S}) induced by the LSSE, respectively. Thus, the thermoelectric voltage can be generated by the combination of the LSSE and ISHE and observed by measuring the voltage V between the ends of the metallic layer, where the sign of V is determined by that of θ_{SH} (see Fig. 2) [44]. This thermoelectric generation mechanism works below the Curie temperature of the magnetic insulator [74]. Here, to detect the LSSE voltage, the thickness of the metallic layer has to be comparable to its spin diffusion length [34], [137], typically a few to several hundreds of nanometers, since the spin current injected into the metallic layer and the resultant \mathbf{E}_{ISHE} exist only in the vicinity of the metal/insulator interface due to the spin relaxation. We also note that, when a highly resistive insulator is used, the contribution from thermoelectric phenomena in itinerant

magnets, such as the conventional Seebeck and Nernst effects, is eliminated in the LSSE device [42], [58].

III. BASIC CHARACTERISTICS OF SPIN SEEBECK DEVICES

In this section, by using the Pt/YIG model systems, we demonstrate the basic characteristics of the LSSE devices, such as the dependence of the thermoelectric voltage on the temperature, temperature gradient and its direction, magnetic field and its direction, and device geometry.

A. Fundamental Experiments

Here, we show the fundamental properties of the LSSE [44], [51], [58]. The Pt/YIG junction system used here consists of a single-crystalline YIG slab and a Pt film sputtered on the well-polished surface of the YIG. The lengths of the Pt film (YIG slab) along the x , y , and z directions are $l_x = 2$ mm ($L_x = 2$ mm), $l_y = 6$ mm ($L_y = 6$ mm), and $l_z = 10$ nm ($L_z = 1$ mm), respectively. To generate ∇T along the z direction, the temperatures of the heat baths attached to the top and bottom of the Pt/YIG-slab sample were stabilized to 300 K and 300 K + ΔT , respectively. The external magnetic field \mathbf{H} (with the magnitude H) was applied to the Pt/YIG-slab sample in the $x - y$ plane at an angle θ to the y direction [see the inset to Fig. 4(a)].

Fig. 4(a) shows V between the ends of the Pt film in the Pt/YIG-slab sample as a function of ΔT at $H = 1.2$ kOe. When \mathbf{H} was applied along the x direction ($\theta = 90^\circ$), the magnitude of V was found to be proportional to ΔT . As shown in Fig. 4(b), the sign of V for finite values of ΔT is reversed in response to the sign reversal of \mathbf{H} , indicating that the V signal in the Pt film is affected by the magnetization direction of the YIG slab (note that the magnetization of the YIG slab is aligned along the \mathbf{H} direction when $H > 0.5$ kOe). To confirm the origin of this signal, we also measured the θ dependence of V in the same Pt/YIG-slab sample at $\Delta T = 10$ K and $H = 1.2$ kOe [Fig. 4(c)]. The V signal was observed to vary with θ in a sinusoidal pattern and vanish when $\theta = 0$ and 180° , a situation consistent with the symmetry of the ISHE induced by the LSSE described in (3).

The above experiments indicate that the observed thermoelectric voltage is attributed to the LSSE. However, to exclusively establish the LSSE, the contribution of the LSSE has to be separated from that of the ANE [6]. Since Pt is a paramagnetic metal and YIG is a very good insulator, the ANE does not exist in the Pt/YIG system in the ordinary sense. In this system, however, weak ferromagnetism may be induced in the Pt layer in the vicinity of the Pt/YIG interface due to a static magnetic proximity effect [183]–[190] because Pt is near the Stoner ferromagnetic instability [191], [192]. In fact, when the thickness of Pt is very thin (< 3 nm), weak ferromagnetic signals were observed by means of X-ray magnetic circular

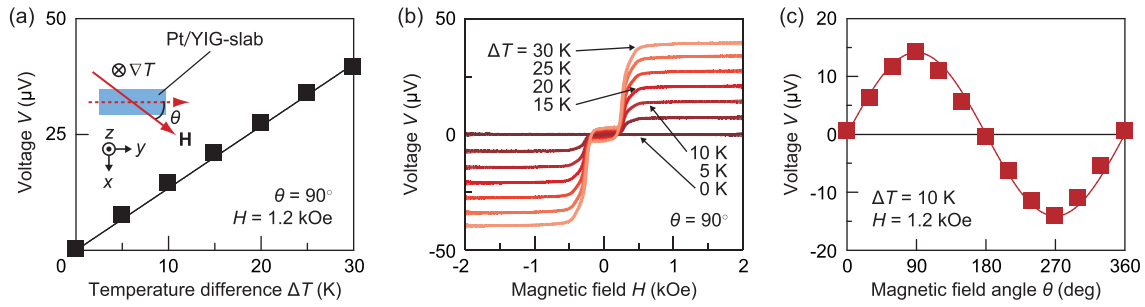


Fig. 4. (a) Temperature-difference ΔT dependence of the voltage V in the Pt/YIG-slab sample at $H = 1.2$ kOe and $\theta = 90^\circ$, measured when $\nabla T \parallel -z$. θ denotes the angle between H and the y direction. (b) H dependence of V in the Pt/YIG-slab sample for various values of ΔT at $\theta = 90^\circ$. (c) θ dependence of V in the Pt/YIG-slab sample at $\Delta T = 10$ K and $H = 1.2$ kOe.

dichroism [184]–[186]. If the proximity-induced ferromagnetism induces the ANE in the Pt layer, the ISHE voltage induced by the LSSE in the Pt/YIG system may be contaminated by the proximity-induced ANE in the Pt layer. This possibility was pointed out by Huang *et al.* in 2012 on the basis of magnetoresistance and Hall measurements [183], although the anisotropic magnetoresistance in Pt/YIG systems was subsequently shown to be attributed to the spin Hall magnetoresistance [158]–[162]. Here, the electric field induced by the ANE is generated according to the relation [44]

$$\mathbf{E}_{\text{ANE}} = \mathcal{N} \mathbf{M} \times \nabla T \quad (4)$$

where \mathcal{N} is the anomalous Nernst coefficient. This configuration is similar to that of the LSSE since \mathbf{E}_{ANE} is generated along the y direction when $\nabla T \parallel z$ and $\mathbf{M} \parallel x$ [compare Fig. 5(a) and (c)]. After the problem presentation by Huang *et al.*, the pure detection of the LSSE was realized by using Au/YIG systems [50], [51], where Au is free from the magnetic proximity effect because its electronic structure is far from the Stoner instability [191]. To investigate the magnetic proximity effect in Pt/YIG systems, microwave spectroscopy measurements were also carried out [187], [190]. Guo *et al.* theoretically investigated the proximity-induced ANE in Pt and Pd within Berry-phase formalism based on relativistic band-structure calculations [189].

The clear separation of the LSSE from the proximity-induced ANE was reported in [51], [58] by comparing transverse thermoelectric voltage in the Pt/YIG system in in-plane magnetized (IM) and perpendicularly magnetized (PM) configurations. In the IM (PM) configuration, H is applied parallel (perpendicular) to the Pt/YIG interface and ∇T is applied perpendicular (parallel) to the interface, as shown in Fig. 5(d) [5(h)]. The IM configuration is the same as the LSSE setup (see Fig. 3), where both the LSSE and ANE can appear if they exist. In the PM configuration, the ANE signal can appear since the

temperature gradient, magnetization, and interelectrode direction are at right angles to one another (4), while the LSSE voltage should disappear due to the symmetry of the ISHE (3), where $\hat{s} \parallel \mathbf{j}_s$ in the PM configuration. Therefore, the quantitative comparison of the voltage between these configurations enables the estimation of the ANE contamination in the Pt/YIG system.

Fig. 5(e) and (i) show the H dependence of the voltage normalized by the device length along the y direction and the temperature gradient in the YIG slab, $V/(L_y \nabla T_{\text{YIG}})$, in the Pt/YIG-slab sample in the IM and PM configurations, respectively [44], [58]. The magnitude of $V/(L_y \nabla T_{\text{YIG}})$ in the IM configuration was found to be much greater than that in the PM configuration. Here, the magnitude of the normal Nernst voltage, which is the H -linear component of $V/(L_y \nabla T_{\text{YIG}})$, in the Pt/YIG-slab sample in the PM configuration is comparable to that in the Pt/paramagnetic $\text{Gd}_3\text{Ga}_5\text{O}_{12}$ (GGG)-slab sample and in a Pt plate without a substrate [58], confirming that the in-plane temperature gradient is generated in the Pt/YIG-slab sample in the PM configuration (note that the Pt/GGG-slab sample exhibits only a normal Nernst effect and no LSSE voltage except at very low temperatures [82]). The voltage behavior in the Pt/YIG-slab sample is completely different from that in a ferromagnetic $\text{Ni}_{81}\text{Fe}_{19}$ film on a GGG substrate, where only the ANE and small normal Nernst effect appear; in the $\text{Ni}_{81}\text{Fe}_{19}$ film, the isotropic ANE voltage was observed in both the IM and PM configurations, when the voltage is normalized by the temperature gradient in the $\text{Ni}_{81}\text{Fe}_{19}$ film [see Fig. 5(g) and (k)] [44], [58]. The above results clearly show that the transverse thermoelectric voltage in the Pt/YIG system is dominated by the ISHE voltage induced by the LSSE and that the proximity-ANE contamination is negligibly small. In [58], the contribution of the proximity-induced ANE voltage in the Pt/YIG system was estimated to be less than 0.1% of the LSSE voltage. As shown in Fig. 5(f) and (j), similar results were obtained in Au/YIG systems.

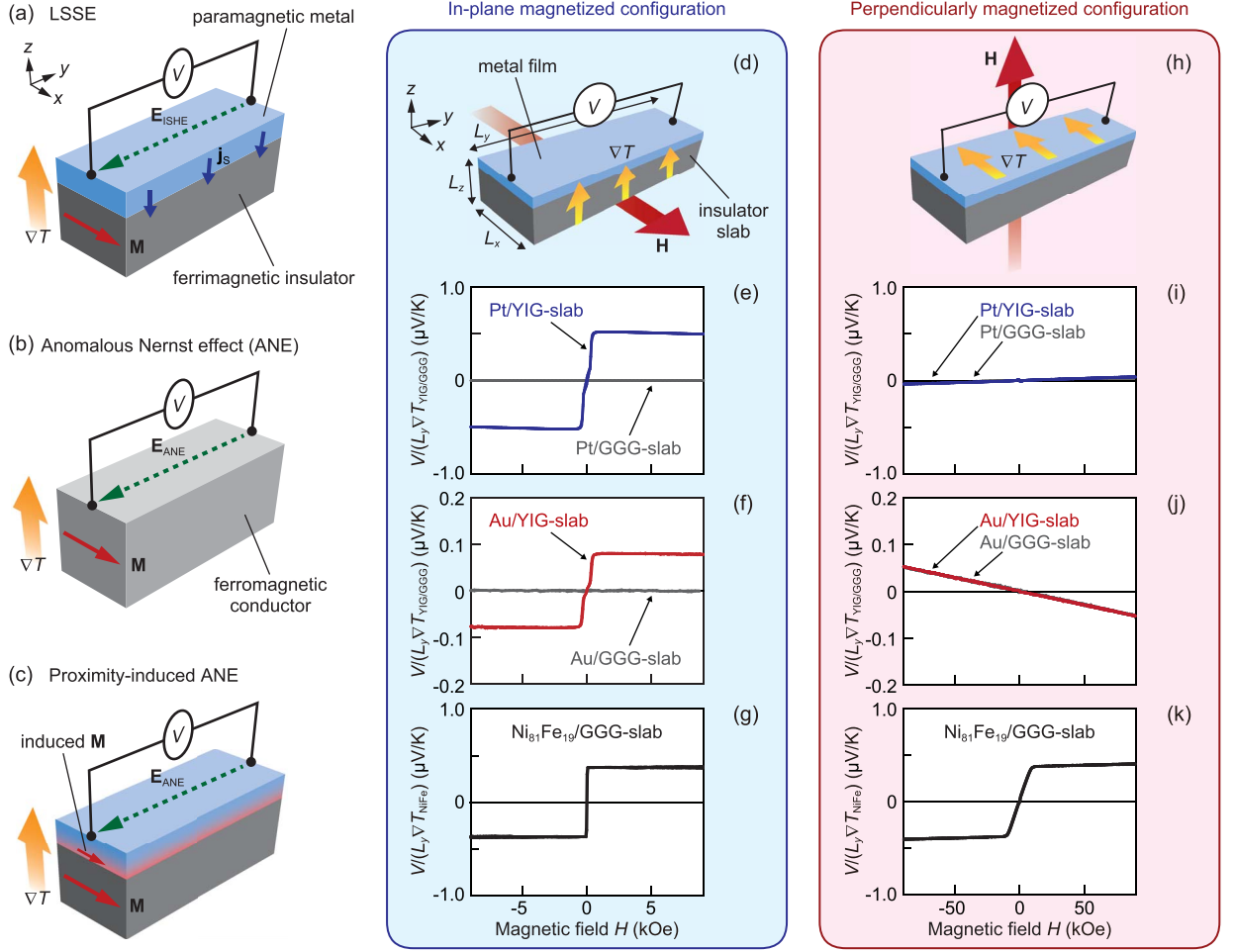


Fig. 5. (a)–(c) Schematic illustrations of the LSSE (a), ANE (b), and proximity-induced ANE (c). E_{ANE} denotes the electric field generated by the ANE. (d) A schematic illustration of the metal-film/insulator-slab junction system in the in-plane magnetized (IM) configuration. (e), (f) H dependence of $V/(L_y \nabla T_{YIG(GGG)})$ in the Pt/YIG (GGG)-slab and Au/YIG (GGG)-slab samples in the IM configuration. (g) H dependence of $V/(L_y \nabla T_{NiFe})$ in the $Ni_{81}Fe_{19}/GGG$ -slab sample in the IM configuration. (h) A schematic illustration of the metal-film/insulator-slab junction system in the perpendicularly magnetized (PM) configuration. (i), (j) H dependence of $V/(L_y \nabla T_{YIG(GGG)})$ in the Pt/YIG (GGG)-slab and Au/YIG (GGG)-slab samples in the PM configuration. (k) H dependence of $V/(L_y \nabla T_{NiFe})$ in the $Ni_{81}Fe_{19}/GGG$ -slab sample in the PM configuration. L_x , L_y , and L_z are the lengths of the insulator slab along the x , y , and z directions, respectively. $\nabla T_{YIG(GGG)}$ and ∇T_{NiFe} denote the temperature gradients in the YIG (GGG) slab and $Ni_{81}Fe_{19}$ film, respectively. The sample consists of a 10-nm-thick Pt, Au, or $Ni_{81}Fe_{19}$ film formed on a single-crystalline YIG or GGG slab. All the measurements were performed at $T = 300$ K.

The experimental results shown in Fig. 5 clearly demonstrate that the thermoelectric voltage in the Pt/YIG system is due entirely to the ISHE induced by the LSSE. Although the separation of the LSSE from the ANE is very important from the viewpoint of fundamental physics, even the proximity-induced ANE should be utilized effectively from the viewpoint of thermoelectric applications because the thermoelectric output of the LSSE device might be enhanced by the superposition of the proximity-induced ANE voltage. Recently, to validate the availability of the proximity-induced ANE, we investigated the ANE in alternately-stacked Pt/Fe multilayer films, which were designed to enhance the proximity-

induced ANE intentionally; the proximity-ANE contribution in the Pt/Fe multilayer films is expected to be up to two orders of magnitude greater than that in the conventional Pt/YIG system [120]. However, even in these multilayer systems, no clear evidence for the existence of the proximity-induced ANE was observed. Therefore, the potential of the magnetic proximity effect as a thermoelectric generation mechanism is still unknown. In contrast, the standard ANE in ferromagnetic materials has already been investigated as a novel thermoelectric conversion technology [118], [121]. Especially, we focus on ferromagnetic metals as conductive layer materials of the LSSE device since they enable the hybrid thermoelectric

generation by the LSSE and ANE [44] and replacement of noble metals, such as Pt and Au, in the LSSE device, as discussed in Section V-C.

B. High Magnetic Field Dependence

Recently, several research groups reported the investigation of the high-magnetic-field response of the LSSE in Pt/YIG systems with different YIG thicknesses at various temperatures [93], [94], [98], [103]. These studies provide a significant guideline for optimizing the thickness of the magnetic insulator layer of the LSSE device since the high-magnetic-field dependence of the LSSE was found to be associated with the characteristic lengths of the LSSE. In this subsection, with showing our experimental results for the Pt/YIG systems [93], we review the behavior of the LSSE in a high magnetic field range and its interpretation.

The observation of the SSE in insulators revealed that the magnon excitation plays a key role in this phenomenon. After the pioneering theoretical work by Xiao *et al.* [166], the SSE is mainly described in terms of the effective magnon temperature T_m in a ferrimagnetic insulator and effective electron temperature T_e in an attached paramagnetic metal; when the effective magnon-electron temperature difference is induced by an external temperature gradient, a spin current is generated across the ferrimagnet/paramagnet interface due to the thermal spin pumping. Subsequently,

Adachi *et al.* developed linear-response theories of the magnon- and phonon-mediated SSEs [167], [168], [172]. Hoffman *et al.* formulated a Landau-Lifshitz-Gilbert theory of the SSE to investigate the thickness dependence and length scale of the SSE [173]. In 2014, Rezende *et al.* discussed the SSE in terms of a bulk magnon spin current created by a temperature gradient in a ferrimagnetic insulator [60]. Furthermore, various theoretical models of the magnon-driven SSE were also developed [169]–[171], [174]–[182]. However, microscopic understanding of the relation between the magnon excitation and thermally generated spin current is yet to be fully established, and more detailed studies are necessary. Since the magnon excitation is modulated by a magnetic field due to the Zeeman gap $g\mu_B H$, the ISHE voltage induced by the SSE can also be affected by the magnetic field. Therefore, systematic measurements of the magnetic-field-induced response of the SSE become powerful tools for unraveling the thermo-spin conversion mechanism based on the magnon excitation.

In Fig. 6(a), we show the transverse thermopower $S(\equiv (V/\Delta T)(L_z/L_y))$ in the Pt/YIG-slab sample as a function of H for several values of the temperature T , measured when H was swept between ± 90 kOe. The clear LSSE voltage was observed in the Pt/YIG-slab sample at all the temperatures and its magnitude at each temperature gradually decreases with increasing H after taking the maximum value, while the magnitude of M is almost

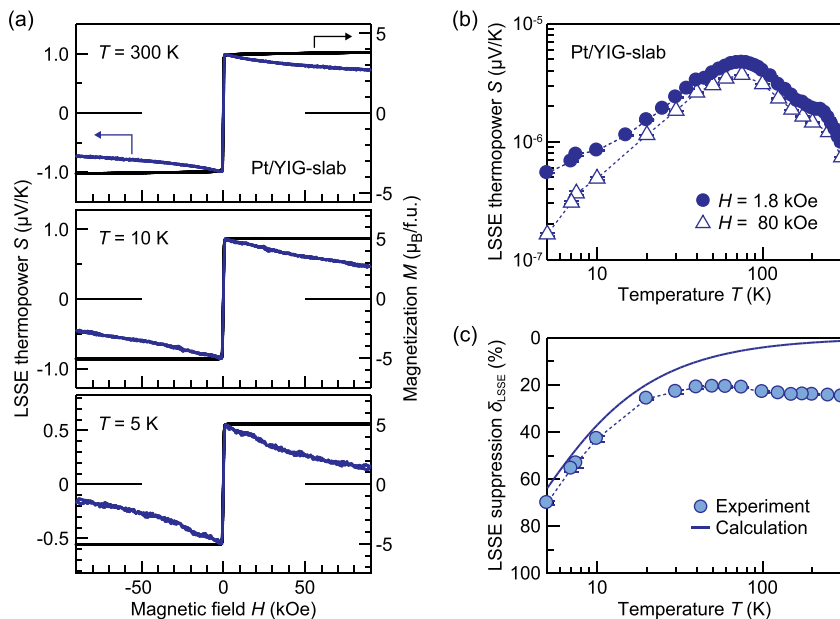


Fig. 6. (a) H dependence of the LSSE thermopower S in the Pt/YIG-slab sample and the magnetization M of the YIG slab at $T = 300$ K, 10 K, and 5 K, measured when H was swept between ± 90 kOe. The sample consists of a 5-nm-thick Pt film sputtered on the top surface of a single-crystalline YIG slab. (b) Double logarithmic plot of the T dependence of S in the Pt/YIG-slab sample at $H = 1.8$ kOe (closed circles) and 80 kOe (open triangles). (c) T dependence of the suppression of the LSSE voltage by magnetic fields δ_{SSE} in the Pt/YIG-slab sample (circles). A blue line shows the T dependence of δ_{SSE} calculated based on the conventional SSE model (see [93] for details).

constant after the saturation. This suppression of the LSSE voltage becomes apparent by applying high magnetic fields, while it is very small in the conventional LSSE measurements in a low field range. The suppression of the LSSE voltage was shown to be irrelevant to the normal Nernst effect in the Pt film [93].

The magnetic-field-induced suppression of the LSSE voltage in the Pt/YIG-slab sample increases with decreasing the temperature. Fig. 6(c) shows the T dependence of the suppression of the LSSE thermopower δ_{SSE} in the same Pt/YIG-slab sample, where δ_{SSE} is defined as $(S_{\text{max}} - S_{80 \text{ kOe}})/S_{\text{max}}$ with S_{max} and $S_{80 \text{ kOe}}$ respectively being the S values at the maximum point and at $H = 80 \text{ kOe}$ [the T dependence of S at the positive H values is shown in Fig. 6(b)]. The field-induced suppression in the Pt/YIG-slab sample was observed to be almost constant above 30 K and strongly enhanced below 30 K; the δ_{SSE} value in the Pt/YIG-slab sample reaches $\sim 70\%$ at $T = 5 \text{ K}$. The field-induced suppression of the LSSE for $T > 30 \text{ K}$ cannot be explained by the conventional SSE models, while that for $T < 30 \text{ K}$ seemingly agrees with numerical calculations based on the thermal spin pumping mechanism [see Fig. 6(c)] (see [93] for details). The inconsistency between the observed suppression of the LSSE voltage and the conventional formulation at relatively-high temperatures is attributed to the fact that the small Zeeman energy is defeated by thermal fluctuations when $g\mu_B H \ll k_B T$ in the conventional models, where g , μ_B , and k_B are the g -factor, Bohr magneton, and Boltzmann constant, respectively (note that the magnon gap energy at $H = 80 \text{ kOe}$ corresponds to $g\mu_B H/k_B = 10.7 \text{ K}$); to affect the magnon excitation by magnetic fields, the magnon energy has to be comparable to or less than the Zeeman energy. In contrast, the observed large suppression of the LSSE voltage in the Pt/YIG-slab sample indicates that the magnon excitation relevant to the LSSE is affected by magnetic fields even at around room temperature. This result suggests that low-frequency magnons of which the energy is comparable to the Zeeman energy provide a dominant contribution to the LSSE; the thermo-spin conversion efficiency of the LSSE has magnon-frequency dependence, which is not included in the conventional SSE theories. In [93] and [193], the origin of this spectral nonuniform thermo-spin conversion is discussed in terms of the frequency dependence of a magnon thermalization (energy relaxation) length and a magnon diffusion length, respectively. It is notable that lower frequency magnons exhibit the longer characteristic lengths in general [126]–[129], [166], [193]–[199].

The above results and discussions indicate that, to maximize the thermoelectric output of the LSSE device, the thickness of the magnetic insulator has to be greater than the characteristic lengths of low-frequency magnons providing a strong contribution to the LSSE, since the contribution from the long-range magnons can be limited

by boundary conditions in thin magnetic insulators [93]. In fact, several research groups demonstrated that, by using the Pt/YIG-slab and Pt/YIG-film systems, the magnitude of the LSSE thermopower monotonically decreases with decreasing the thickness of YIG [our experimental results are shown in Fig. 7(a) and (b)] [93], [95], [103]. Significantly, the suppression of the LSSE by high magnetic fields, δ_{SSE} , also monotonically decreases with decreasing the YIG thickness [see Fig. 7(a) and (c)]. This behavior indicates that the contribution of low-frequency magnons, which govern the LSSE suppression in the Pt/YIG-slab sample, fades away in the Pt/YIG-film samples when the YIG thickness is less than their characteristic lengths and that only remaining contribution from high-frequency magnons, which have energy much greater than the Zeeman energy and provide a weak contribution to the LSSE, appears in the thin YIG-film samples. As reviewed in this subsection, the measurements of the high-magnetic-field response of the LSSE are useful for characterizing the properties of the LSSE devices associated with magnon excitation.

C. Current-Voltage-Power Characteristics and Scaling Law

Now we demonstrate the current-voltage-power characteristics of the LSSE device by using a Pt/BiY₂Fe₅O₁₂

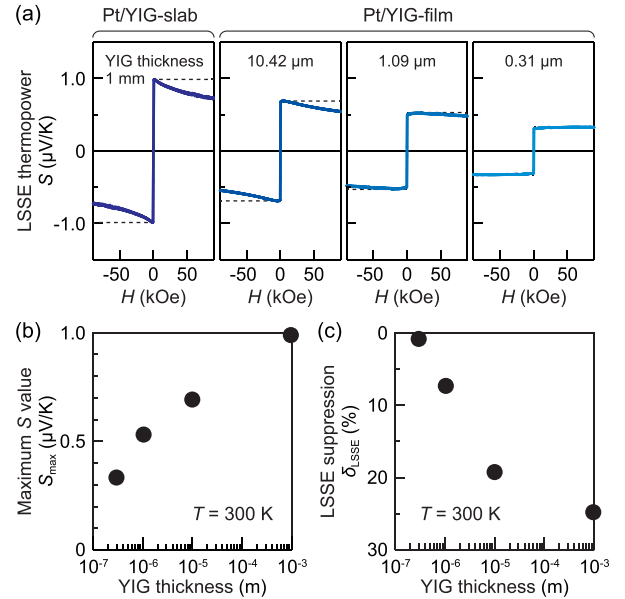


Fig. 7. (a) H dependence of S in the Pt/YIG-slab sample with the YIG thickness of 1 mm and in the Pt/YIG-film samples with the YIG thickness of 10.42 μm , 1.09 μm , and 0.31 μm at $T = 300 \text{ K}$, measured when H was swept between $\pm 90 \text{ kOe}$. The YIG films were grown on single-crystalline GGG substrates by a liquid phase epitaxy method. (b) YIG-thickness dependence of S_{max} at $T = 300 \text{ K}$. (c) YIG-thickness dependence of δ_{SSE} at $T = 300 \text{ K}$.

(Bi:YIG) bilayer film [44]. To determine the characteristics, we attached a load resistance R_{load} to the Pt layer and measured the voltage across the load resistance V_{load} to estimate the output power $V_{\text{load}}^2/R_{\text{load}}$ with changing the R_{load} value, while most of the LSSE experiments have been performed under the open-circuit condition. In Fig. 8(a), we show $V_{\text{load}}^2/R_{\text{load}}$ generated from the Pt/Bi:YIG-film sample at $\Delta T = 11.2$ K as a function of R_{load} . We found that the maximum output power can be extracted when R_{load} is equal to the internal resistance of the Pt layer: $R_{\text{Pt}} = 33 \Omega$. This behavior is also confirmed by the linear current-voltage relation and parabolic current-power relation for the Pt/Bi:YIG-film sample in Fig. 8(b). The current-voltage-power characteristics and optimizing condition for the load resistance for the LSSE devices are the same as those for any linear generators, such as batteries and conventional thermoelectric modules.

Next, we experimentally verify the scaling law of the LSSE device: the output power is proportional to the device area, introduced in Section I. To do this, we investigated the dependence of the LSSE voltage on the size, i.e., length and width, of the metallic layer of the LSSE device as follows [101].

For measuring the metallic-layer-length dependence of the LSSE, we used the structure called “spin Hall thermopile” [49]. The spin Hall thermopile consists of an alternating array of two different metallic wires with different spin Hall angles, connected in series in a zig-zag configuration. The sample used here is the spin Hall thermopile comprising 10-nm-thick Pt wires and 30-nm-thick Au wires formed on a Bi:YIG film [see the inset to Fig. 8(c)]. In this sample, the LSSE voltage in each wire is integrated into the total voltage between the ends of the Pt-Au thermopile and the total voltage predominantly comes from the Pt wires, because the spin Hall angle and resistivity of Pt are greater than those of Au and the thickness of the Pt wires is less than that of the Au wires (note that the magnitude of the LSSE voltage increases with decreasing the thickness of the metallic layer except for ultrathin regions [58], [64], [69]). Fig. 8(c) shows the dependence of the LSSE voltage per unit temperature difference, $V/\Delta T$, on the total length of the Pt wires l_y^{tot} in the Pt-Au thermopile, where l_y^{tot} is changed by changing the number of the Pt-Au pairs. As expected above, the magnitude of $V/\Delta T$ increases in proportion to l_y^{tot} .

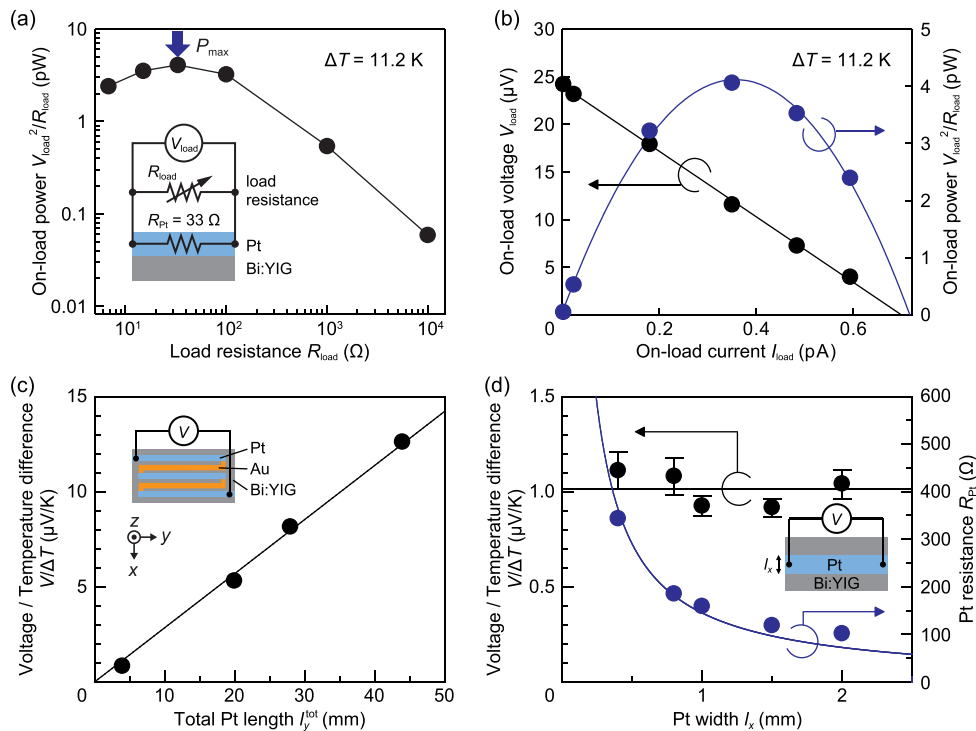


Fig. 8. (a) On-load power $V_{\text{load}}^2/R_{\text{load}}$ induced by the LSSE in the Pt/Bi:YIG-film sample as a function of the load resistance R_{load} at $\Delta T = 11.2$ K. V_{load} denotes the on-load voltage. (b) V_{load} and $V_{\text{load}}^2/R_{\text{load}}$ induced by the LSSE in the Pt/Bi:YIG-film sample as a function of the on-load current $I_{\text{load}} = V_{\text{load}}/R_{\text{load}}$. The Pt/Bi:YIG-film sample used for the experiments (a) and (b) consists of a 10-nm-thick Pt film with the size of $16 \times 16 \text{ mm}^2$ and a 120-nm-thick Bi:YIG film formed on a 0.5-mm-thick SGGG wafer of 1-inch diameter. (c) $V/\Delta T$ as a function of the total Pt length l_y^{tot} in the [Pt-Au thermopile]/Bi:YIG-film samples. (d) $V/\Delta T$ and the Pt-film resistance R_{Pt} as a function of the Pt width l_x in the Pt/Bi:YIG-film samples. All the measurements were performed at room temperature.

In addition to the Pt-length dependence, we also investigated the Pt-width dependence. We fabricated Pt films with different widths on fixed-size Bi:YIG films, where the length and thickness of the Pt films are fixed [see the inset to Fig. 8(d)]. In Fig. 8(d), $V/\Delta T$ and the Pt-film resistance R_{Pt} are plotted as a function of the Pt width l_x . We found that the magnitude of $V/\Delta T$ is almost independent of l_x , while R_{Pt} is inversely proportional to l_x .

The obtained scaling results, i.e., $V/\Delta T \propto l_y^{\text{tot}}$ and $V/(R_{\text{Pt}}\Delta T) \propto l_x$, clearly indicate that a larger film area leads to larger thermoelectric output power that can be extracted to an external load. Here, we would like to emphasize again that the scaling law of the LSSE devices is quite different from that of conventional thermoelectric devices based on the Seebeck effect, where the thermoelectric output scales with the number of thermocouples connected in series (see Section I and Fig. 1).

IV. THEORY OF EFFICIENCY OF SPIN SEEBECK THERMOELECTRIC DEVICES

In this section, we present a theory of the efficiency of thermoelectric devices based on the LSSE. First, we give a brief review of the efficiency of thermoelectric generators based on the ANE. This is because the ANE has a similarity to the LSSE in that the induced electric field is orthogonal to the applied temperature gradient, and a thermoelectric device possessing this characteristic is called a transverse device [5]. Next, based on the discussion of the ANE generators, we formulate the efficiency of the LSSE devices.

A. Review of Efficiency of Thermoelectric Generators Based on Anomalous Nernst Effects

As pointed out above, it is quite instructive to review the efficiency calculation of the ANE device [200]–[202]. We begin with the following transport equations [203]:

$$\mathbf{E} = \rho \mathbf{j} + \alpha \nabla T + \mathcal{N} \mathbf{M} \times \nabla T \quad (5)$$

$$\mathbf{q} = \Pi \mathbf{j} - \kappa \nabla T + \mathcal{N} \mathbf{T} \mathbf{M} \times \mathbf{j} \quad (6)$$

where \mathbf{E} , \mathbf{j} , and \mathbf{q} are an applied electric field, charge current density (with the magnitude j), and heat current density, respectively. $\Pi = \alpha T$ is the Peltier coefficient. The (anomalous) Hall coefficient is disregarded as it is irrelevant to the present discussion, and the Leduc-Righi coefficient [204], [205] is assumed to be negligibly small. Here we note that the following discussion is applicable not only to the ANE devices but also to normal Nernst devices [6] if the spontaneous magnetization is replaced with an external magnetic field, while this article focuses on the comparison between the LSSE and ANE devices because of their similar characteristics. It should also be added that the thermoelectric conversion efficiency of

normal Nernst generators, or Ettingshausen coolers, in semimetals can be much greater than that of the ANE and LSSE devices, although an external magnetic field must be applied [206].

We first calculate the amount of heat evolved per unit time and volumes, which governs the temperature profile of the system in the steady state. This quantity is given by $-\nabla \cdot \mathbf{q}_E$ [203], where $\mathbf{q}_E = \mathbf{q} + \phi \mathbf{j}$ is the energy current density with ϕ being the electrochemical potential. Using (5) and (6), we obtain

$$-\nabla \cdot \mathbf{q}_E = \rho j^2 + \kappa \nabla^2 T - T \mathbf{j} \cdot \nabla \alpha + 2\mathcal{N}(\mathbf{j} \times \mathbf{M}) \cdot \nabla T \quad (7)$$

where the first and second terms on the right hand side represent the Joule heating and thermal conduction. The third term, which comes from the temperature dependence of the Seebeck coefficient via the relation $\nabla \alpha = (d\alpha/dT)\nabla T$, is the Thompson effect and will be neglected hereafter to simplify the argument. Besides, since the last term can be interpreted as a change in the Thompson effect due to the presence of magnetization [203], this term is also discarded. Therefore, by considering the conservation law of energy flux, i.e., $\nabla \cdot \mathbf{q}_E = 0$, we obtain the following equation:

$$\rho j^2 + \kappa \nabla^2 T = 0 \quad (8)$$

which determines the temperature distribution in thermoelectric devices, known as Domenicali's equation [207].

Let us focus on the ANE device shown in Fig. 9(a). Here, a temperature gradient $\nabla_z T = -\Delta T/l_z$ ($\Delta T = T_h - T_c$) is applied along the z axis, and an external magnetic field is applied along the x axis to align the magnetization, $\mathbf{M} = M_S \hat{x}$. Under the isothermal condition ($\nabla_y T = 0$) as well as the open circuit condition ($j = 0$), the ANE induces an electric field $E_y = \mathcal{N} M_S \Delta T/l_z$ along the y axis, and a charge current density is driven in the y direction, i.e., $\mathbf{j} = j_y \hat{y}$. Since the electromotive force is given by

$$V_{\text{emf}} = -\mathcal{N} M_S \Delta T \left(\frac{l_y}{l_z} \right) \quad (9)$$

and the total resistance in the circuit is given by $R_{\text{tot}} = R + R_{\text{load}}$ with R and R_{load} respectively being the internal and load resistances, the resultant charge current $\mathbf{I} = I_y \hat{y}$ is calculated to be

$$I_y = \frac{V_{\text{emf}}}{R_{\text{tot}}} = \frac{-\mathcal{N} M_S \Delta T \left(\frac{l_y}{l_z} \right)}{R(1+r)} \quad (10)$$

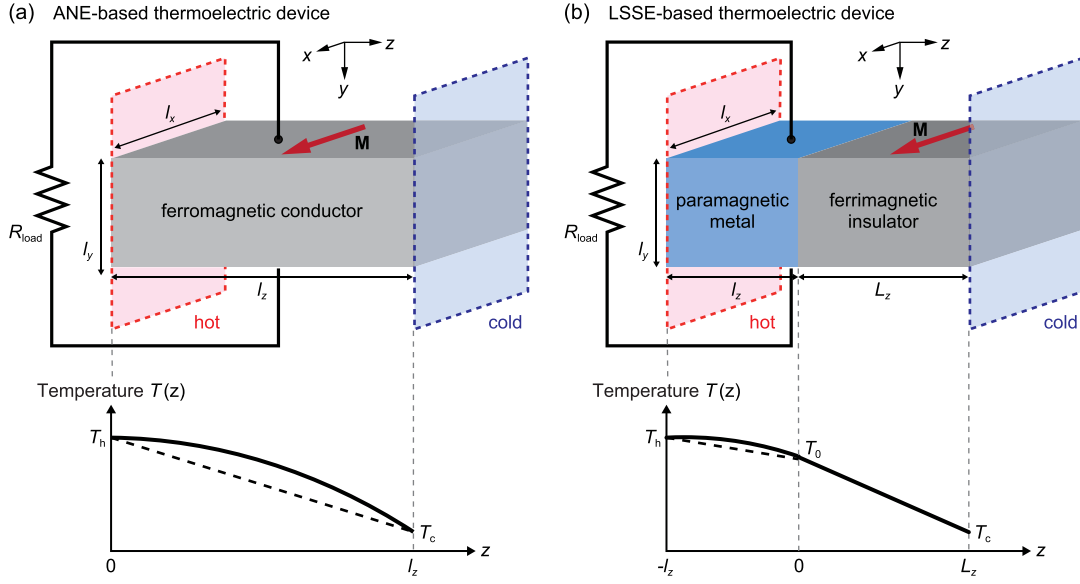


Fig. 9. (a) Schematic illustration of the ANE-based thermoelectric device and its temperature profile along the z direction. (b) A schematic illustration of the LSSE-based thermoelectric device and its temperature profile along the z direction. The load resistance R_{load} is attached to the ferromagnetic conductor (paramagnetic metal) of the ANE (LSSE) device. l_x , l_y , and l_z are the lengths of the ferromagnetic conductor (paramagnetic metal) of the ANE (LSSE) device along the x , y , and z directions, respectively. $T_{h(c)}$ is the temperature at the hot (cold) end of the devices and T_0 is the temperature at the metal/insulator interface of the LSSE device.

where we have introduced a dimensionless variable $r \equiv R_{load}/R$.

Now we discuss the efficiency of the ANE device. The efficiency is defined by

$$\eta_{ANE} = \frac{P_{out}}{Q_h} \quad (11)$$

where $P_{out} = R_{load}I_y^2$ is the electrical power output and Q_h is the thermal power input from the hot reservoir. The latter quantity is calculated as follows [208], [209]. First, we assume a uniform charge current distribution along the z direction, i.e., $j_y(z) = j = \text{constant}$. Then, from Domenicali's equation (8) under the condition $T(z=0) = T_h$ and $T(z=l_z) = T_c$, the temperature distribution is calculated to be

$$T(z) = T_h - \left(\frac{z}{l_z}\right)\Delta T + \left(\frac{\rho_j^2}{2\kappa}\right)z(l_z - z) \quad (12)$$

where the distribution of $T(z)$ is schematically shown in Fig. 9(a). Next, we evaluate the magnitude of the heat current at the hot reservoir, i.e., $q_h = \mathcal{N}M_S Tj - \kappa(\nabla_z T)_{z=0}$, using (6). Then, the rate of heat removal

from the hot reservoir, defined by $Q_h = (l_x l_y)q_h$, is calculated to be

$$Q_h = \frac{\mathcal{N}M_S T_h}{\left(\frac{l_z}{l_y}\right)} I_y + K\Delta T - \frac{R}{2} I_y^2 \quad (13)$$

where $K = \kappa(l_x l_y / l_z)$ is the thermal conductance in the z direction and $R = \rho(l_y / l_x l_z)$ is the electrical resistance in the y direction.

From (11)–(13), the efficiency is expressed as a function of $r = R_{load}/R$

$$\eta_{ANE} = \eta_C f(r) \quad (14)$$

where $\eta_C = \Delta T / T_h$ is the Carnot efficiency. Here, the characteristic function

$$f(r) = \frac{r}{-(1+r) + \frac{(1+r)^2}{Z'_{ANE} T_h} - \frac{\Delta T}{2T_h}} \quad (15)$$

is defined by the isothermal figure of merit

$$Z'_{ANE} = \frac{(\mathcal{N}M_S)^2}{\kappa' \rho} \quad (16)$$

Table 1 Parameters That Influence the Efficiency of the LSSE Thermoelectric Generators

θ_{SH}	Spin Hall angle of P
α_S	Spin Seebeck coefficient [Eq. (26)]
κ_F	Total thermal conductivity of F
ρ_P	Electrical resistivity of P
l_z	Thickness of P
L_z	Thickness of F
σ_P	Electrical conductivity of P, $\sigma_P = 1/\rho_P$ [Eq. (20)]
σ_m	Magnon conductivity of F [Eq. (23)]
c_1	Ratio of spin current injected into P to thermal drift magnon current in F [Eq. (25)]
c_2	Ratio of spin current injected back into F to spin-Hall drift current in P [Eq. (28)]
λ	Spin diffusion length of P
Λ	Magnon diffusion length of F

where κ' is the thermal conductivity at zero electric field. Note the minus sign in the first term of the denominator in (15), which is peculiar to transverse devices [200]. By maximizing η_{ANE} with respect to r , the optimized efficiency η_{ANE}^* in the limit of $\Delta T \ll T_h$ is calculated to be

$$\eta_{ANE}^* = \eta_C \left(\frac{1 - r^*}{1 + r^*} \right) \quad (17)$$

$$r^* = \sqrt{1 - Z'_{ANE} T_h} \quad (18)$$

where the functional form is quite different from the conventional Seebeck device because of the fact that the ANE device has a symmetry of transverse devices. Note that, by contrast, the maximum power output is given by the impedance matching condition $R = R_{load}$ as is well known [208].

Two comments are in order. First, according to the argument of [210] and [211], the isothermal figure of merit $Z'_{ANE} T$ in (15) is related to the adiabatic figure of merit $Z_{ANE} T = (\mathcal{N} M_S)^2 / \kappa \rho$ as

$$Z'_{ANE} T = \frac{Z_{ANE} T}{1 + Z_{ANE} T} \quad (19)$$

such that $0 \leq Z'_{ANE} T \leq 1$, where κ is the thermal conductivity at zero charge current. Therefore, the maximum allowed efficiency is obtained for $Z'_{ANE} T = 1$ (i.e., $r^* = 0$), achieving the Carnot efficiency: $\eta_{ANE}^{\max} = \eta_C$. Second, the figure of merit Z'_{ANE} in (16) is determined by the thermal conductivity κ' and the electrical resistivity ρ that are defined in the same material.

B. Efficiency of Thermoelectric Generators Based on Spin Seebeck Effects

In this subsection, based on the discussion in the previous subsection, we discuss the efficiency of the LSSE device. We consider a device shown in Fig. 9(b), where a bilayer of a paramagnetic metal P and a ferrimagnetic insulator F is sandwiched between hot and cold reservoirs. We assume that the thermal conductivity of P κ_P is much greater than that of F κ_F , such that the temperature

gradient develops inside F and thus the temperature gradient inside P is negligibly small in comparison to F. Looking at Table 1 given in [212], this assumption seems moderately reasonable. Note that we made this assumption in order to keep the mathematical manipulations manageable and to extract a simple analytical expression; otherwise such a simple result would never be obtained and a more involved numerical approach would be required, which is beyond our scope. Also, we assume that there is no discontinuous jump in the temperature distribution at the P/F interface. In this sense, the present approach is complementary to the calculation in [130], where only the temperature difference at the P/F interface was considered as a driving force. Instead, we assume that the temperature is a smooth function across the P/F interface, and the temperature at the interface T_0 is determined by the heat current conservation. Here, the relationship between the present continuous temperature model and a three temperature model used in [57], [130], and [166] is given in the following way. The present approach is constructed based on the formalism developed in [196], and the magnon accumulation (see Eq. (11) of [196]) corresponds to the effective magnon-phonon temperature difference. It has been demonstrated that the present single temperature gradient model provides us with an excellent description of the SSE in magnetic multilayers [100].

We start our discussion from the following transport equations for P:

$$\mathbf{j} = \sigma_P \mathbf{E} + \theta_{SH} \hat{\mathbf{s}} \times \mathbf{j}_S \quad (20)$$

$$\mathbf{j}_S = \sigma_P \mathbf{E}_S + \theta_{SH} \hat{\mathbf{s}} \times \mathbf{j} \quad (21)$$

$$\mathbf{q} = -\kappa_P \nabla T \quad (22)$$

where \mathbf{E}_S is the spin voltage gradient and σ_P is the electrical conductivity of P. For F, we assume the following transport equations:

$$\mathbf{j}_S = \sigma_m \mathbf{E}_S - \zeta_m \nabla T \quad (23)$$

$$\mathbf{q} = \Pi_m \mathbf{j}_S - \kappa_F \nabla T \quad (24)$$

where \mathbf{E}_S in F is determined by the magnon density gradient ∇n_m , σ_m is the magnon conductivity, and ζ_m (Π_m) is the magnon Seebeck (Peltier) coefficient. Here, the thermal conductivity $\kappa_F = \kappa_F^{\text{mag}} + \kappa_F^{\text{ph}}$ of F includes both magnon contribution κ_F^{mag} as well as phonon contribution κ_F^{ph} , and Onsager's reciprocity [212] requires $\Pi_m = \zeta_m T / \sigma_m$.

Let us first calculate the open circuit voltage under a temperature bias $\Delta T = T_h - T_c$ between the hot and cold reservoirs. As stated before, because of the condition $\kappa_P \gg \kappa_F$, the temperature gradient develops inside F as $\nabla T = -[(T_h - T_0)/L_z]\hat{\mathbf{z}} \approx -(\Delta T/L_z)\hat{\mathbf{z}}$. According to (23), this temperature gradient drives a spin current $\mathbf{j}_S = \zeta_m(\Delta T/L_z)\hat{\mathbf{z}}$ inside F, which then injects an amount of

$$\mathbf{j}_S = c_1 \zeta_m \left(\frac{\Delta T}{L_z} \right) \hat{\mathbf{z}} \quad (25)$$

into P, where the coefficient c_1 ($0 < c_1 < 1$) represents the ratio of the spin current injected into P to the thermal drift magnon current in F. Note that the parameter c_1 is proportional to the spin mixing conductance. If we adopt an approach of [60] and [196] where the continuity of \mathbf{j}_S at the P/F interface is postulated, the constant c_1 is given by $c_1 \propto [\cosh(L_z/\Lambda) - 1]/\sinh(L_z/\Lambda)$, where Λ is the magnon diffusion length of F. Inside P, thanks to the ISHE (20), the injected spin current $\mathbf{j}_S = [c_1(\zeta_m \Delta T)/L_z]\hat{\mathbf{z}}$ is converted into a charge current $\mathbf{j} = -[\theta_{\text{SH}} c_1 \zeta_m \Delta T/L_z]\hat{\mathbf{y}}$ when $\hat{\mathbf{s}} = \hat{\mathbf{x}}$. Then, in the open circuit condition, this current is compensated by an electromotive force

$$V_{\text{emf}} = -\theta_{\text{SH}} \alpha_S \Delta T \left(\frac{L_y}{L_z} \right) \quad (26)$$

where $\alpha_S = (1/2)c_1 \zeta_m / \sigma_P$. Here, the factor 1/2 in α_S comes from averaging over the thickness of P, where we approximated the hyperbolic variation of $j_S(z)$ by a linear curve by assuming that the thickness of P is of the order of its spin diffusion length λ ($\sim L_z$). For a circuit containing the total resistance $R_{\text{tot}} = R + R_{\text{load}}$, the current $\mathbf{I} = I_y \hat{\mathbf{y}}$ driven by the open circuit voltage (26) is given by

$$I_y = -\frac{\theta_{\text{SH}} \alpha_S \Delta T \left(\frac{L_y}{L_z} \right)}{R(1+r)} \quad (27)$$

where $r = R_{\text{load}}/R$ as before. Owing to (21), the resultant charge current density $\mathbf{j} = [I_y/(l_x l_z)]\hat{\mathbf{y}}$ drives an additional

spin current $\delta \mathbf{j}_S = [(\theta_{\text{SH}} I_y)/(l_x l_z)]\hat{\mathbf{z}}$, a part of which is injected back into F. Then, due to (24), this spin current is accompanied by a heat current

$$\delta \mathbf{q} = c_2 \frac{\Pi_m \theta_{\text{SH}} I_y}{(l_x l_z)} \hat{\mathbf{z}} \quad (28)$$

where the coefficient c_2 ($0 < c_2 < 1$) represents the ratio of the spin current injected back into F to the spin-Hall drift current δj_S in P. Note that the heat current accompanied by the spin current given in (25), i.e., $\mathbf{q} = \Pi_m c_1 \zeta_m (\Delta T/L_z)\hat{\mathbf{z}}$, is absorbed into the definition of κ_F as $\kappa_F - \Pi_m c_1 \zeta_m \rightarrow \kappa_F$.

Now we can calculate the thermal power input Q_h from the hot reservoir. We assume that Domenicali's equation (8) approximately holds for P, neglecting spin Joule heating [213]. Using heat current conservation at the P/F interface, we have $q_h = \kappa_F (\Delta T/L_z) - |\delta \mathbf{q}| - \rho_P j^2$, where $\rho_P = 1/\sigma_P$. From this, we have

$$Q_h = K_F \Delta T + c_2 \Pi_m T \left(\frac{l_y}{l_z} \right) I_y - R I_y^2 \quad (29)$$

for $Q_h = (l_x l_y) q_h$. At the same time, the output power is given by

$$P_{\text{out}} = R_{\text{load}} I_y^2 \quad (30)$$

so that after a lengthy but straightforward calculation, the efficiency $\eta_{\text{SSE}} = P_{\text{out}}/Q_h$ is obtained

$$\eta_{\text{SSE}}(r) = \eta_C g(r) \quad (31)$$

where the characteristic function $g(r)$ is defined by

$$g(r) = \frac{r}{\left(\frac{L_z}{l_z} \right) \frac{(1+r)^2}{Z_{\text{SSE}} T_h} - \left(\frac{L_z}{l_z} \right) \xi(1+r) - \frac{\Delta T}{T_h}} \quad (32)$$

$$\xi = \left(\frac{c_2}{c_1} \right) \left(\frac{\sigma_P}{\sigma_m} \right) \quad (33)$$

and the figure of merit of the LSSE device Z_{SSE} is given by

$$Z_{\text{SSE}} = \frac{(\theta_{\text{SH}} \alpha_S)^2}{\kappa_F \rho_P}. \quad (34)$$

By maximizing η_{SSE} with respect to r , the optimized efficiency in the limit of $\Delta T \ll T_h$ is calculated to be

$$\eta_{\text{SSE}}^* = \eta_c \left(\frac{l_z}{L_z} \right) \frac{1}{\xi} \left(\frac{1 - r^*}{1 + r^*} \right) \quad (35)$$

$$r^* = \sqrt{1 - \xi Z_{\text{SSE}} T_h} \quad (36)$$

where the functional form again has a characteristic of transverse devices. Note that, because the result is quite different from that of [130] and several important steps to arrive at the final result therein are missing, we must conclude that it is almost impossible for us to draw parallel between the two approaches. In Table 1, we summarize parameters that influence the efficiency of the LSSE thermoelectric generators.

C. Discussion

First of all, it is important to note that, in comparison with the ANE device [(16)], the figure of merit of the LSSE device is determined by the thermal conductivity κ_F and the electrical resistivity ρ_P that are defined in two different materials, reflecting the fact that the charge current flows only through P whereas the thermal resistance is mainly given by F. Therefore, in contrast to Z'_{ANE} of the ANE device, Z_{SSE} of the LSSE device is free from the limitation of the Wiedemann-Franz law.

The optimized efficiency η_{SSE}^* is determined by three factors: the figure of merit Z_{SSE} , the spin converting parameter ξ , and the geometrical factor l_z/L_z . Thus, for the calculation of η_{SSE}^* , we need to estimate the magnitude of ξ [see (33)], in addition to the Z_{SSE} value. The parameter ξ may be evaluated in the following way. First, since both the parameters c_1 and c_2 measure the ratio of a spin injection current to a bulk spin current, we could set $c_2/c_1 \approx 1$ for a rough estimate (a microscopic determination of the factor c_2/c_1 is beyond our scope since the present discussion is devoted to a phenomenological description of the efficiency). Next, the conductivity ratio may be estimated using Einstein relations, $\sigma_P = e^2 D_P g_P(\epsilon_F)$ and $\sigma_m = e^2 D_m n_m / (k_B T)$, where D_P and D_m are, respectively, the electron diffusion coefficient of P and magnon diffusion coefficient of F, $g_P(\epsilon_F)$ is the electron density of states per unit volume at the Fermi energy, and n_m is the magnon number density. With these estimates, we obtain

$$\xi \approx \left(\frac{D_P}{D_m} \right) \frac{g_P(\epsilon_F)}{\frac{n_m}{(k_B T)}} \quad (37)$$

where n_m can be calculated by $n_m = \int d\epsilon g_m(\epsilon) f_{\text{BE}}(\epsilon)$ with the magnon density of states per unit volume $g_m(\epsilon)$ and the Bose-Einstein distribution function $f_{\text{BE}}(\epsilon)$.

Now we discuss the upper limit of the efficiency η_{SSE}^* . Similarly to the isothermal figure of merit of the ANE device [see (19)], the isothermal LSSE figure of merit is expected to satisfy $0 \leq Z_{\text{SSE}} T \leq 1$. Then, the maximum allowed efficiency of the LSSE device (35) is achieved for $r^* = 0$ (i.e., $\xi Z_{\text{SSE}} T_h = 1$), which yields

$$\eta_{\text{SSE}}^{\text{max}} = \eta_c \left(\frac{l_z}{L_z} \right) \frac{1}{\xi}. \quad (38)$$

Note that the existence of such a maximum allowed efficiency requires a condition that $0 \leq 1/\xi \leq 1$; otherwise the situation $r^* = 0$ cannot be realized. Note also that, although at first glance it appears that a use of a thin magnetic layer ($L_z \ll l_z$) would result in a very large efficiency, this naive expectation does not work since $1/\xi$ is proportional to L_z/Λ for $L_z/\Lambda \ll 1$. Anyway, as is obvious from the structure of the present calculation, the efficiency of the LSSE device is bound by the constraint of the second law of thermodynamics. Therefore, there must be a condition $(l_z/L_z)(1/\xi) \leq 1$ to ensure that the upper limit of the maximum allowed efficiency is the Carnot efficiency, a microscopic derivation of which is left to future studies. However, the efficiency of present LSSE devices is still very low; making use of typical values for Pt/YIG systems: $l_z = 10$ nm, $L_z = 1$ μ m, $\rho_P = 0.1$ $\mu\Omega$ m, $\kappa_F = 7$ W/mK, $\theta_{\text{SH}\alpha_S} = 1$ μ V/K, and $\xi = 1$, the figure of merit and the ratio of the optimized efficiency to the Carnot efficiency are respectively estimated to be $Z_{\text{SSE}} T = 4 \times 10^{-4}$ and $\eta_{\text{SSE}}^*/\eta_c = 1 \times 10^{-4}\%$ at $T = 300$ K, where η_{SSE}^* has a very little dependence on ξ when $\xi Z_{\text{SSE}} T \ll 1$. Therefore, the dramatic enhancement of the LSSE thermopower and the reduction of thermal conductivity of F are necessary for realistic thermoelectric applications of the LSSE. The determination of the optimum geometrical factor, l_z/L_z , is also important for improving the efficiency, while the increase of l_z/L_z may conflict with the thickness dependence of the LSSE because the LSSE thermopower usually decreases with increasing l_z [50], [58], [64], [69], [91] and decreasing L_z [43], [93], [95], [98], [103].

V. DEMONSTRATIONS FOR THERMOELECTRIC APPLICATIONS

In this section, we introduce several approaches for future thermoelectric applications of the LSSE devices, which include the demonstration of the LSSE-based thermoelectric generation in coating films, flexible devices, all-ferromagnetic devices, and multilayer films. The former two structures are under development to exploit the versatility and scalability of the LSSE devices, while the latter two are to improve their thermoelectric performance.

A. Spin Thermoelectric Coating

The concept of a coating-based LSSE device called “spin thermoelectric (STE) coating” was first proposed in 2012 [43]. The STE-coating device consists of a metal/magnetic insulator bilayer film directly coated on a heat source. Thanks to the simple structure and straightforward scaling law of the LSSE, the STE coating is potentially applicable to the implementation of large-area thermoelectric devices onto various-shaped heat sources, such as the surfaces of electronic instruments and automobile bodies.

The STE coating was demonstrated by using a spin-coating method, which may realize large-area thermoelectric devices in a highly productive way. Here, we used Bi:YIG and Pt as the magnetic insulator and metallic film layers, respectively. The STE-coating films were formed by using the simple fabrication steps illustrated in Fig. 10(a). First, a Bi:YIG film was formed on a $(\text{GdCa})_3(\text{GaMgZr})_5\text{O}_{12}$ (substituted gadolinium gallium garnet: SGGG) substrate, which has good lattice-matching properties with Bi:YIG, by means of a metal-organic decomposition (MOD) method [43]. The MOD method consists of simple three step processes: spin coating, drying, and annealing of the MOD

solution containing the constituent elements, which enables the fabrication of thin magnetic insulator films without using specialized and costly equipment, such as vacuum deposition apparatus. Subsequently, the Pt film was formed by sputtering over the whole surface of the Bi:YIG film. The thicknesses of the Bi:YIG and Pt films are 120 nm and 10 nm, respectively. Importantly, although the surface area of the samples used here is small ($8 \times 2 \text{ mm}^2$), the above process can be easily applied to large-area manufacturing, since it does not require patterning steps such as photolithography and electron-beam lithography.

In Fig. 10(b) and (c), we, respectively, show the ΔT and H dependences of V in the Pt/Bi:YIG STE-coating film. The clear LSSE voltage was found to appear even in this thin film structure prepared by the MOD coating method. We also checked that no signal appears in a plain Pt film sputtered directly on a SGGG substrate, indicating that the thin Bi:YIG film works as a thermoelectric generator. We found that a crystalline Bi:YIG film can be grown even onto a glass substrate by using the MOD method [43], and the STE coating is applicable even onto amorphous surfaces. Such versatile implementation of thermoelectric functions may open opportunities for various applications making full use of omnipresent heat.

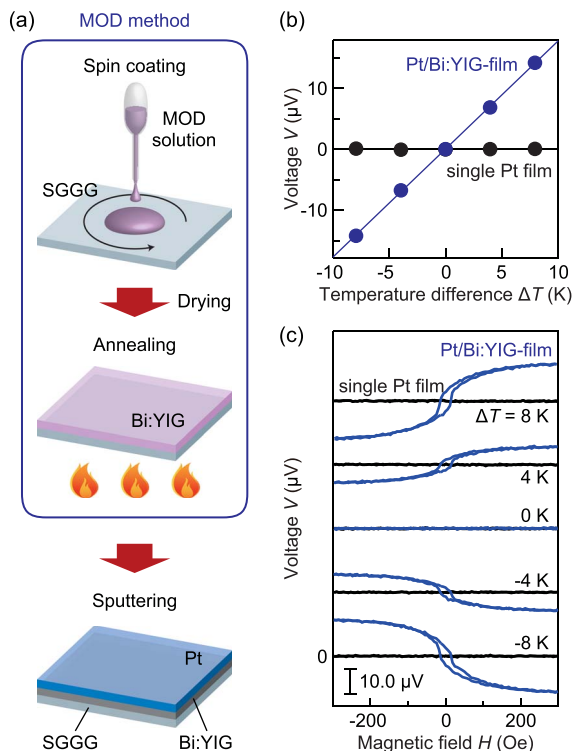


Fig. 10. (a) Preparation process for the Pt/Bi:YIG STE-coating device. (b) ΔT dependence of V in the Pt/Bi:YIG-film sample and single Pt film. (c) H dependence of V in the Pt/Bi:YIG-film sample and single Pt film for various values of ΔT . All the measurements were performed at room temperature.

B. Flexible Spin Seebeck Devices

Most of the conventional thermoelectric devices are rigid, and not easily applicable onto curved or uneven heat sources. Because the conventional thermoelectric device consists of a number of II-structured thermocouples connected electrically in series, it is vulnerable to bending stresses, making it difficult to construct flexible devices. In contrast, the LSSE device has a high affinity for flexible thermoelectric generation owing to its simple structure and scaling law; it will be applicable on various heat sources, paving the way to versatile thermoelectric generators or sensors.

Recently, we demonstrated the construction of a LSSE-based flexible thermoelectric sheet [106]. To construct the flexible LSSE device, we used spray-coating technique called “ferrite plating” [214], [215], which enables the fabrication of ferrimagnetic ferrite thin films. Since conventional ferrite-film preparation techniques, including sputtering [85], liquid phase epitaxy [139], and pulsed laser deposition [135], require high temperature processes (ranging from 400°C to 800°C) for crystallizing ferrites, they cannot be used for the formation of ferrite films on heat-labile soft materials, such as plastics. By contrast, the ferrite plating method is based on chemical reaction processes, and thus does not need any high temperature processes, enabling the coating of ferrite films on a variety of substrates including flexible plastic films.

The fabrication process of the ferrite plating method is very simple, which also requires no specialized and costly equipment. As schematically illustrated in Fig. 11(a), the ferrite film can be grown simply by spraying an aqueous reaction solution and an oxidizer simultaneously onto a substrate, mounted on a rotating heating stage [214], [215]. The thickness of the ferrite film can be controlled by the spray volume and time and can be dependent on surface conditions of substrates. Importantly, all the processes of the ferrite plating method can be performed below 100 °C, applicable to heat-labile plastic substrates.

By using the ferrite plating method, we successfully fabricated the flexible thermoelectric sheet based on the LSSE [see a photograph in Fig. 11(b)]. The flexible LSSE device consists of a ferrimagnetic $\text{Ni}_{0.2}\text{Zn}_{0.3}\text{Fe}_{2.5}\text{O}_4$ thin film, grown on a flexible polyimide substrate by the ferrite plating, and a Pt film, sputtered on the $\text{Ni}_{0.2}\text{Zn}_{0.3}\text{Fe}_{2.5}\text{O}_4$ film. As shown in Fig. 11(b), the Pt/ $\text{Ni}_{0.2}\text{Zn}_{0.3}\text{Fe}_{2.5}\text{O}_4$ /polyimide sheet is highly flexible and bendable. We observed clear LSSE signals in the flexible thermoelectric sheet, where the magnitude of the LSSE signals is comparable to that in the conventional rigid LSSE devices [106]. We also demonstrated that the ferrite plating method is applicable to not only plastic substrates but also glass substrates; it is useful for constructing low-cost LSSE devices.

A noticeable feature of the ferrite film grown by the ferrite plating method is its columnar grain structure [see the cross-sectional scanning electron microscope image of the $\text{Ni}_{0.2}\text{Zn}_{0.3}\text{Fe}_{2.5}\text{O}_4$ film in Fig. 11(c)]. Here, the

crystal orientation of $\text{Ni}_{0.2}\text{Zn}_{0.3}\text{Fe}_{2.5}\text{O}_4$ is coherently aligned within each columnar grain [106]. Such columnar structure can be suitable for the flexible LSSE devices because of the following two reasons. First, in the LSSE configuration, the spin current is generated along the columnar structure, and thus less affected by grain scattering. Second, the columnar grain boundary can work as a stress-relieving cushion when the film is bent, leading to the high flexibility and bending tolerance.

The ferrite plating method potentially enables the direct coating of thermoelectric functions onto various surfaces over a large area, expanding the versatility and utility of the LSSE devices. Significantly, the flexible thermoelectric sheet based on the LSSE, demonstrated here, has remarkably low thermal resistance because of the thick-substrate-free structure. Therefore, it may be suitable for heat-flow sensing applications [106].

C. Hybrid Thermoelectric Generation Based on Spin Seebeck and Anomalous Nernst Effects

As shown in Fig. 2, most of the LSSE experiments to date have been performed by using Pt as a metallic layer. Pt is useful for investigating the physics of the LSSE, since it enables sensitive detection of the thermally generated spin currents and the spin-current-related parameters, such as the spin diffusion length and spin Hall angle, of Pt have been well studied [34]. However, Pt is unsuitable for thermoelectric applications of the LSSE because of its high material cost. Furthermore, even the spin-charge conversion efficiency of Pt is insufficient for obtaining adequate thermoelectric performance.

Recently, the ISHE has been investigated not only in paramagnetic materials but also in ferromagnetic materials by means of the LSSE experiments [56], [58], [61], [70], [87], [96] (see Fig. 2). The main purpose of these studies is microscopic understanding of the ISHE in ferromagnets. In contrast, we focus on ferromagnetic materials as low-cost replacements for Pt in the LSSE devices. Here, as a simple model case, we consider a ferromagnetic metal/ferrimagnetic insulator junction system under a temperature gradient. In this system, the ANE is induced in the ferromagnetic metal layer in a conventional manner. In addition to the ANE contribution, if the spin current is injected into the ferromagnetic metal from the ferrimagnetic insulator via the LSSE and the ISHE appears in the ferromagnetic metal, the hybrid thermoelectric generation based on the combination of the LSSE and ANE is realized [see Fig. 12(a)]. The previous studies showed that the direction of \mathbf{E}_{ISHE} is the same as that of \mathbf{E}_{ANE} in various ferromagnetic materials [56], [58], [61], [70], [87], [96]. Even when the spin Hall angle of the ferromagnetic metal is smaller than that of Pt, the shortfall of the ISHE voltage can be compensated by the superposition of the ANE voltage. In fact, the thermoelectric output of all-ferromagnetic

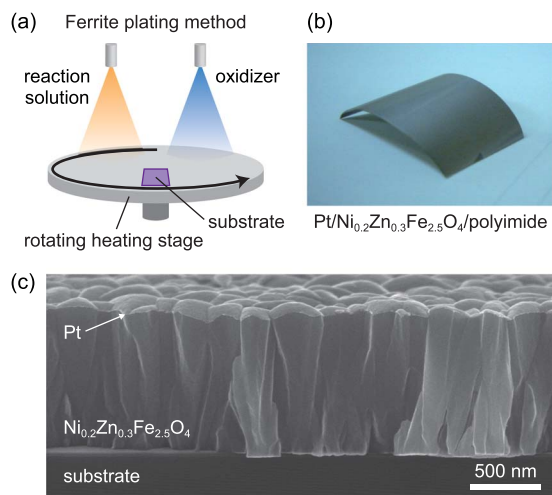


Fig. 11. (a) Schematic illustration of the ferrite-plating method. (b) A photograph of a LSSE-based flexible thermoelectric sheet, where a Pt/ $\text{Ni}_{0.2}\text{Zn}_{0.3}\text{Fe}_{2.5}\text{O}_4$ film was formed on a 25- μm -thick polyimide flexible substrate. (c) A scanning electron microscope image of a $\text{Ni}_{0.2}\text{Zn}_{0.3}\text{Fe}_{2.5}\text{O}_4$ film grown on a thermally oxidized silicon substrate by the ferrite-plating method.

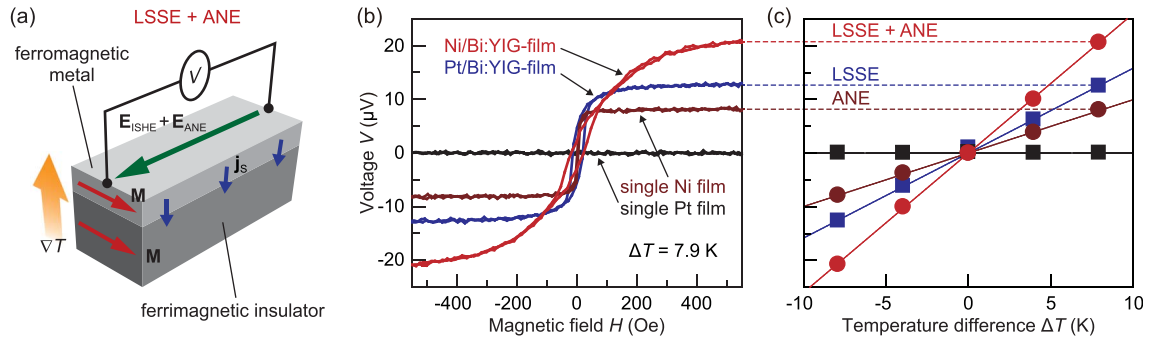


Fig. 12. (a) Schematic illustration of the hybrid thermoelectric generation based on the LSSE and ANE in a ferromagnetic metal/ferrimagnetic insulator junction system. (b) H dependence of V in the Ni/Bi:YIG-film sample, Pt/Bi:YIG-film sample, single Ni film, and single Pt film at $\Delta T = 7.9$ K. (c) ΔT dependence of V in the Ni/Bi:YIG-film sample, Pt/Bi:YIG-film sample, single Ni film, and single Pt film. The thicknesses of the Ni, Pt, and Bi:YIG films are 10 nm, 10 nm, and 120 nm, respectively. All the measurements were performed at room temperature.

devices can even be better than that of the conventional Pt-based devices, as demonstrated below.

In Fig. 12(b) and (c), we compare the transverse thermoelectric voltage between ferromagnetic Ni/Bi:YIG-film and conventional Pt/Bi:YIG-film systems. The Bi:YIG layer of the Ni/Bi:YIG-film and Pt/Bi:YIG-film samples were formed on a SGGG substrate by means of the MOD method. We found that the Ni/Bi:YIG-film sample exhibits the clear V signal of which the magnitude is more than twice greater than that of the ANE voltage in a plain Ni film directly placed on the substrate, indicating that the signal in the Ni/Bi:YIG-film sample is attributed to the superposition of the ANE in the Ni layer and the ISHE induced by the spin current injected from the Bi:YIG layer. Importantly, the magnitude of V in the Ni/Bi:YIG-film sample is even greater than that in the conventional Pt/Bi:YIG-film sample [see Fig. 12(b) and (c)]. Since the electrical resistivity of Ni is comparable to or smaller than that of Pt, the Ni/Bi:YIG-film sample shows the better thermoelectric performance than the Pt/Bi:YIG-film sample in terms of not only the output voltage but also the output current or power. This result suggests that the hybrid thermoelectric generation using ferromagnetic metal/ferrimagnetic insulator junction systems will be useful for constructing noble-metal-free, low-cost, and efficient LSSE devices.

D. Spin Seebeck Effect in Multilayer Devices

To realize efficient thermal spin-current generation, the LSSE has recently been investigated in multilayer systems comprising alternately-stacked paramagnet (P)/ferromagnet (F) films [88], [89], [100]. The recent studies have revealed that the LSSE voltage in $[P/F] \times n$ systems significantly and monotonically increases with increasing the number of the P/F bilayers n . For example, in [100], the magnitude of the LSSE voltage in $[Pt/Fe_3O_4] \times 6$ systems was observed to be enhanced by a factor of 4–6 compared with that in $[Pt/Fe_3O_4] \times 1$

bilayer systems (see Fig. 13). Since this LSSE-voltage enhancement is unaccompanied by the increase of the internal resistance, the output power also increases with

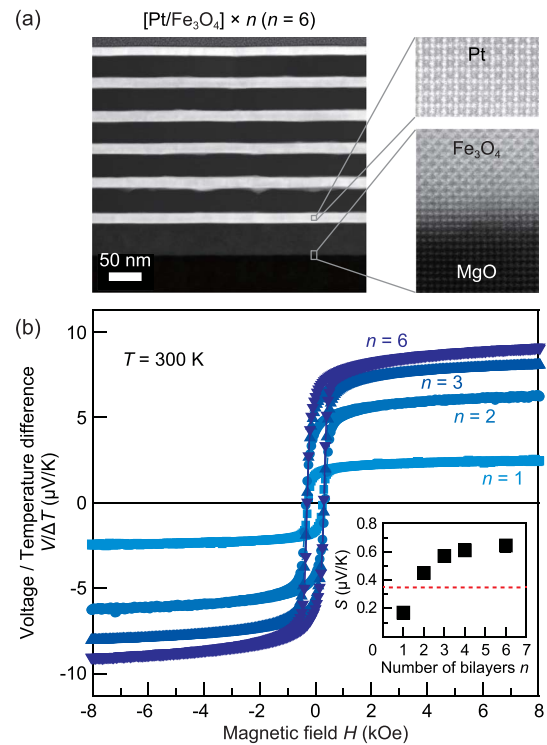


Fig. 13. (a) Scanning transmission electron microscope image of the cross section of the $[Pt/Fe_3O_4] \times 6$ system, where the thickness of the Pt (Fe_3O_4) layers is 17 nm (34 nm). The magnified views of the Pt layer and Fe_3O_4 /MgO interface show the high crystalline quality of the multilayers. (b) H dependence of $V/\Delta T$ in the $[Pt/Fe_3O_4] \times n$ systems for various values of the Pt/ Fe_3O_4 -bilayer number n at $T = 300$ K. The inset to (b) shows the n dependence of S in the $[Pt/Fe_3O_4] \times n$ systems. The red dotted line represents the upper limit of the LSSE voltage for the parallel circuit of connected Pt/ Fe_3O_4 bilayers.

increasing n , a situation different from the case of the LSSE-voltage enhancement by the spin Hall thermopile [44], [49]. The observed n dependence of the LSSE voltage in the $[P/F] \times n$ multilayer systems is beyond conventional expectations based on the situation that the systems are merely regarded as several independent P/F bilayers electrically connected in parallel, where the output voltage is not enhanced while the output power is enhanced owing to the reduction of the internal resistance [Fig. 14(a)] [100]. Importantly, this LSSE-voltage enhancement cannot be explained even when the spin-current injection into P from both the top and bottom F layers is taken into account, where the upper limit of the LSSE enhancement is twice of the voltage in the single P/F bilayer; as shown in Fig. 13(b), the observed enhancement is much greater than this upper limit.

Our current interpretation of the mechanism of the LSSE enhancement in the P/F multilayer systems is summarized as follows [100]. The essence of the LSSE enhancement is the boundary conditions for spin currents flowing normal to the P/F interfaces, which affect the magnitude and spatial profile of the spin currents generated by the LSSE. Here we assume the following two boundary conditions: 1) spin currents must disappear at

the top and bottom surfaces of the multilayer systems; and 2) spin currents in the P and F layers are continuous at the interfaces. Although spin currents in paramagnetic metals and ferrimagnetic insulators are respectively carried by conduction electrons and spin waves, the boundary condition 2) allows us to treat these spin currents in the same manner in the following phenomenological discussions. Let us now compare a spin-current profile in a $P_1/F_1/P_2/F_2$ system with that in a $F_1/P_2/F_2$ system without the top P layer (P_1) [see Fig. 14(b)], where P_1 and P_2 are good spin sinks. According to the boundary condition (i), the spin current is eliminated at the top of the F_1 layer in the $F_1/P_2/F_2$ system. However, this is not the case for the $P_1/F_1/P_2/F_2$ system; the spin current remains a large value at the P_1/F_1 interface, while it must disappear at the top of the P_1 layer. As shown in Fig. 14(b), this difference results in the enhancement of the spin currents near the P_1/F_1 interface, a situation consistent with the prediction in [173]. By applying the above discussion, we calculated out-of-plane spin-current profiles in the $[P/F] \times n$ systems for various values of n [see Fig. 14(c)] and the n dependence of the spin-current magnitude averaged over all the P layers $\langle j_s \rangle$ [the inset to Fig. 14(c)] (note that $\langle j_s \rangle$ can be regarded as an

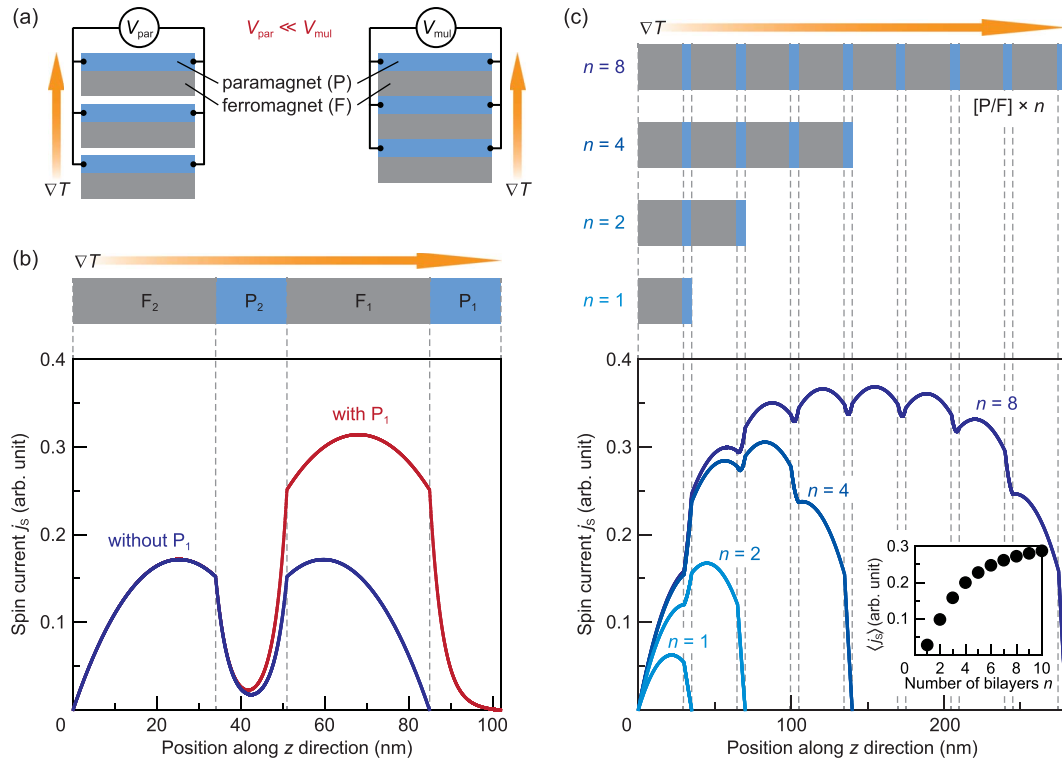


Fig. 14. (a) Comparison of the LSSE voltage between paramagnet (P)/ferromagnet (F) bilayers electrically connected in parallel and an alternately-stacked P/F multilayer film. The LSSE voltage in the latter V_{mul} was found to be much greater than that in the former V_{par} . (b) Comparison of the spin-current j_s profiles between $P_1/F_1/P_2/F_2$ and $F_1/P_2/F_2$ systems. (c) j_s profiles calculated for the $[P/F] \times n$ multilayer systems for various values of the P/F-bilayer number n . The inset to (c) shows the n dependence of the spin-current magnitude averaged over all the P layers $\langle j_s \rangle$. The discussion on these calculation results is detailed in [100].

observable quantity in the measurements of the LSSE in the P/F multilayer systems, since the P layers are electrically connected with each other due to the small thickness and resultant small out-of-plane electrical resistance of the F layers [100]). Importantly, the magnitude of $\langle j_s \rangle$ monotonically increases with increasing n . The physics behind is that, thanks to the multilayer structure, the spin current in the P interlayers acquires a new length scale and boundary value. This phenomenological interpretation is consistent with the experimental results; similar n dependence of the LSSE voltage was observed in the $[\text{Pt}/\text{Fe}_3\text{O}_4] \times n$ systems [compare the inset to Fig. 13(b) with that to Fig. 14(c)] [100]. The $[\text{Pt}/\text{Fe}_3\text{O}_4] \times 6$ system holds the current record of the LSSE thermopower at room temperature (Fig. 15). Since the enhancement of the LSSE based on this mechanism strongly depends on the spin diffusion length (magnon diffusion length) of the P (F) layer, the determination of optimum thicknesses of each layer and optimum P/F material combination is crucial for further improvement of the thermoelectric performance of the LSSE devices.

VI. CONCLUSION AND PROSPECTS

In this article, we reviewed the experimental results of the LSSE in insulator-based systems from the viewpoint of thermoelectric applications. The basic structure of the LSSE device is a simple bilayer film comprising a

magnetic insulator and a metallic or other conductive material; an out-of-plane temperature gradient in the magnetic insulator layer induces an in-plane electric field in the metallic layer via spin-current generation across the interface. Owing to this configuration, the LSSE device exhibits the following unique characteristics. Firstly, the figure of merit of the LSSE device is free from the Wiedemann–Franz law, and can be optimized by selecting the combination of a magnetic insulator with low thermal conductivity and a metallic film with low electrical resistivity. Secondly, the LSSE device follows the convenient scaling law; the maximum extractable power of the LSSE device is proportional to the device area, and can be enhanced simply enlarging the device without constructing complicated modules. The simple structure and scaling law of the LSSE device make it possible to implement thermoelectric functions onto various heat sources by using versatile and low-cost fabrication processes.

The thermoelectric performance of the LSSE device cannot be simply compared with that of conventional thermoelectric devices based on the Seebeck effect because of the different device configurations and driving principles. The theory presented in Section IV shows that the thermoelectric conversion efficiency of the LSSE device is characterized by the figure of merit $Z_{\text{SSE}}T$, described by (34). Here, $Z_{\text{SSE}}T$ is defined as proportional to the square of the LSSE thermopower and inversely proportional to the thermal conductivity of a magnetic insulator and electrical

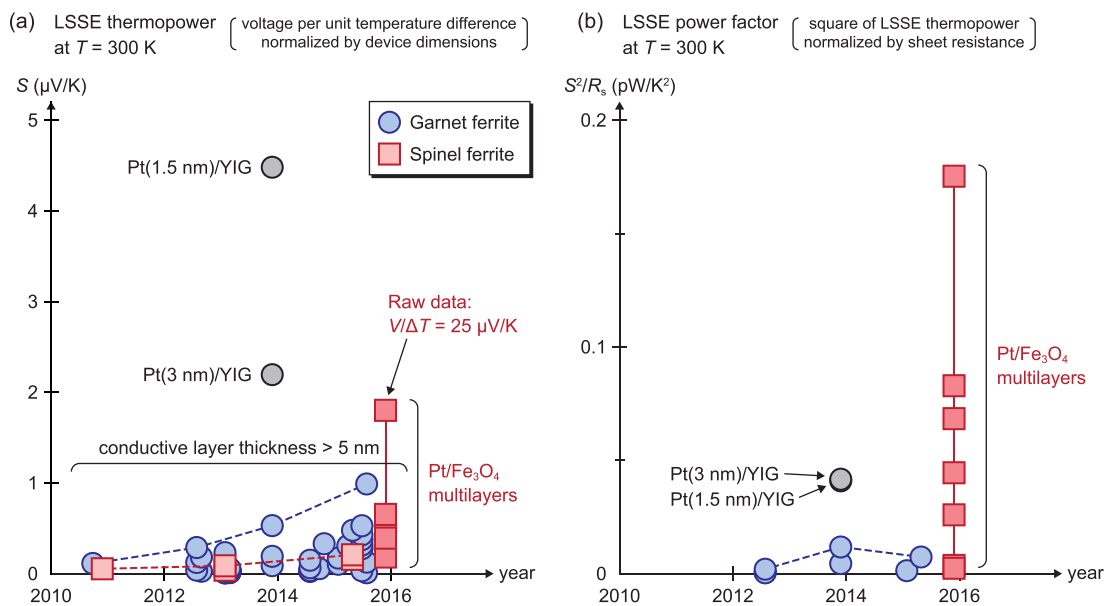


Fig. 15. Time-series trends of the LSSE thermopower S (a) and the LSSE power factor S^2/R_s (b) at $T = 300$ K in the typical LSSE devices [42]–[44], [46], [49], [51], [53]–[55], [58], [71], [74], [80], [81], [85], [90], [92], [93], [100], [120]. Although the output voltage can be increased simply by reducing the conductive layer thickness of the LSSE devices, such thin films cannot exhibit high output power due to their high internal resistance (see gray circle data points). For fair comparison, the experimental data for the LSSE devices with the spin Hall thermopiles are not shown in these trends. For example, in [44], the large LSSE voltage of $V/\Delta T \sim 0.4$ mV/K was realized by using the Pt–Au thermopile structure, although its internal resistance is very high.

resistivity of a metallic film, which is similar to the case of the conventional thermoelectric devices. However, the figure of merit of the LSSE device is defined in the range of $0 \leq Z_{\text{SSE}}T \leq 1$, which is a characteristic of transverse thermoelectric devices.

Despite the potential advantages of the LSSE device, the current stage of the SSE research is still far from realistic thermoelectric applications. This is mainly because the LSSE thermopower is very small at present, although there is plenty of scope for the performance improvement. The LSSE thermopower can be enhanced by improving the thermal spin-current generation efficiency in the magnetic insulator, spin Hall angle in the metallic layer, and spin mixing conductance at the metal/insulator interface. In fact, owing to the efforts after the discovery of the LSSE, the thermoelectric performance of the LSSE device is being improved, especially, in recent years with the advent of multilayer systems as shown in the time-series trends of the LSSE thermopower S [see Fig. 15(a)] and the LSSE power factor [see Fig. 15(b)] in typical LSSE devices. Here, we define the LSSE power factor as the output power normalized by the applied temperature gradient and by the device area

$$\frac{S^2}{R_S} = \left(\frac{V L_z}{\Delta T L_y} \right)^2 \frac{l_y}{R l_x} = \frac{V^2}{R} \frac{1}{\nabla T^2} \frac{1}{l_x l_y} \quad (39)$$

where $R_S (= R l_x / l_y)$ is the sheet resistance of the metallic layer of the LSSE device and we assume $l_{x(y)} = L_{x(y)}$. Fig. 15(b) emphasizes again that multilayer systems are useful for improving the output power of the LSSE device due to the combination of the voltage enhancement and internal resistance reduction. Nevertheless, since even the current record of the thermoelectric performance of the LSSE is still inadequate, continuous development of the LSSE-based thermoelectric technology is necessary. For realistic thermoelectric applications, the reduction of the thermal conductivity (electrical resistivity) of the insulator layer (metallic layer) for the im-

provement of $Z_{\text{SSE}}T$ and optimum thermal design for the stable and continuous operation of the LSSE device are also indispensable.

In the field of spintronics, in addition to the SSE, a variety of novel phenomena in which the interplay of spin and heat plays a crucial role were discovered [6], [25]. Some of the thermo-spin phenomena, such as spin-dependent Seebeck effects [216], [217], Seebeck effects in magnetic tunnel junctions [218], and magnon-drag effects [219], are also potentially applicable to thermoelectric generation in nano-structured spintronics devices. Furthermore, at low temperatures, giant thermopower was observed in transverse SSE devices comprising non-magnetic semiconductors [220]. Although the origin of this giant thermoelectric effect is different from the SSE discussed in this article, it represents a great potential of spin-based thermoelectric technologies. However, these thermo-spin phenomena appear only in conductors; the utilization of insulators is an exclusive feature of the SSE-based thermoelectric generation. We anticipate that this unique feature of the SSE will lead to various thermoelectric applications, including energy harvesters, thermometers, infrared sensors, position detectors [47], and user-interface devices. ■

Acknowledgment

The authors would like to thank M. H. Aguirre, M. Akimoto, P. A. Algarabel, A. Anadón, J. Barker, G. E. W. Bauer, S. R. Boona, C. L. Chien, S. Daimon, S. T. B. Goennenwein, J. P. Heremans, B. Hillebrands, T. Hioki, D. Hou, S. Y. Huang, M. R. Ibarra, J. Ieda, R. Iguchi, K. Ihara, Y. Iwasaki, H. Jin, X. F. Jin, D. Kikuchi, M. Kläui, S. Kohmoto, K. Kondo, I. Lucas, T. Manako, A. Matsuba, A. Miura, L. Morellón, T. Murakami, R. C. Myers, Y. Nakamura, T. Niizeki, T. Nonaka, J. Ohe, Y. Ohnuma, Y. Oikawa, T. Ota, T. Oyake, Z. Qiu, R. Ramos, S. M. Rezende, K. Sato, T. Seki, J. Shiomi, Y. Shiomi, H. Someya, S. Takahashi, K. Takanashi, Y. Tserkovnyak, B. J. van Wees, J. Xiao, N. Yamamoto, and A. Yagmur for their valuable discussions.

REFERENCES

- [1] F. J. DiSalvo, "Thermoelectric cooling and power generation," *Science*, vol. 285, no. 5428, pp. 703–706, Jul. 1999.
- [2] L. E. Bell, "Cooling, heating, generating power, recovering waste heat with thermoelectric systems," *Science*, vol. 321, no. 5895, pp. 1457–1461, Sep. 2008.
- [3] P. Sundarraj, D. Maity, S. S. Roy, and R. A. Taylor, "Recent advances in thermoelectric materials and solar thermoelectric generators—A critical review," *RSC Adv.*, vol. 4, no. 87, pp. 46860–46874, Sep. 2014.
- [4] D. M. Rowe, Ed., *CRC Handbook of Thermoelectrics*. Boca Raton, FL, USA: CRC Press, 1995.
- [5] H. J. Goldsmid, *Introduction to Thermoelectricity*. Berlin, Germany: Springer-Verlag, 2009.
- [6] S. R. Boona, R. C. Myers, and J. P. Heremans, "Spin caloritronics," *Energy Environ. Sci.*, vol. 7, no. 3, pp. 885–910, Mar. 2014.
- [7] L.-D. Zhao, S.-H. Lo, Y. Zhang, H. Sun, G. Tan, C. Uher, C. Wolverton, V. P. Dravid, and M. G. Kanatzidis, "Ultralow thermal conductivity and high thermoelectric figure of merit in SnSe crystals," *Nature*, vol. 508, no. 7496, pp. 373–377, Apr. 2014.
- [8] J. P. Heremans, "Thermoelectricity: The ugly duckling," *Nature*, vol. 508, no. 7496, pp. 327–328, Apr. 2014.
- [9] L. D. Hicks and M. S. Dresselhaus, "Effect of quantum-well structures on the thermoelectric figure of merit," *Phys. Rev. B*, vol. 47, no. 19, pp. 12727–12731, May 1993.
- [10] A. I. Hochbaum, R. Chen, R. D. Delgado, W. Liang, E. C. Garnett, M. Najarian, A. Majumdar, and P. Yang, "Enhanced thermoelectric performance of rough silicon nanowires," *Nature*, vol. 451, no. 7175, pp. 163–167, Jan. 2008.
- [11] B. Poudel, Q. Hao, Y. Ma, Y. Lan, A. Minnich, B. Yu, X. Yan, D. Wang, A. Muto, D. Vashaee, X. Chen, J. Liu, M. S. Dresselhaus, G. Chen, and Z. Ren, "High-thermoelectric performance of nanostructured bismuth antimony telluride bulk alloys," *Science*, vol. 320, no. 5876, pp. 634–638, May 2008.

- [12] A. J. Minnich, M. S. Dresselhaus, Z. F. Ren, and G. Chen, "Bulk nanostructured thermoelectric materials: Current research and future prospects," *Energy Environ. Sci.*, vol. 2, no. 5, pp. 466–479, May 2009.
- [13] J.-F. Li, W.-S. Liu, L.-D. Zhao, and M. Zhou, "High-performance nanostructured thermoelectric materials," *NPG Asia Mater.*, vol. 2, no. 4, pp. 152–158, Oct. 2010.
- [14] P. E. Hopkins, C. M. Reinke, M. F. Su, R. H. Olsson, III, E. A. Shaner, Z. C. Leseman, J. R. Serrano, L. M. Phinney, and I. El-Kady, "Reduction in the thermal conductivity of single crystalline silicon by phononic crystal patterning," *Nano Lett.*, vol. 11, no. 1, pp. 107–112, Jan. 2011.
- [15] M. Kashiwagi, S. Hirata, K. Harada, Y. Zheng, K. Miyazaki, M. Yahiro, and C. Adachi, "Enhanced figure of merit of a porous thin film of bismuth antimony telluride," *Appl. Phys. Lett.*, vol. 98, no. 2, pp. 023114/1–023114/3, Jan. 2011.
- [16] J. Maire and M. Nomura, "Reduced thermal conductivities of Si one-dimensional periodic structure and nanowire," *Jpn. J. Appl. Phys.*, vol. 53, no. 6S, pp. 06JE09/1–06JE09/4, Jun. 2014.
- [17] A. Miura, S. Zhou, T. Nozaki, and J. Shiomi, "Crystalline-amorphous silicon nanocomposites with reduced thermal conductivity for bulk thermoelectrics," *ACS Appl. Mater. Interfaces*, vol. 7, no. 24, pp. 13484–13489, Jun. 2015.
- [18] D. T. Morelli, J. Heremans, M. Sakamoto, and C. Uher, "Anisotropic heat conduction in diacetylenes," *Phys. Rev. Lett.*, vol. 57, no. 7, pp. 869–872, Aug. 1986.
- [19] A. A. Balandin, "Thermal properties of graphene and nanostructured carbon materials," *Nature Mater.*, vol. 10, no. 8, pp. 569–581, Aug. 2011.
- [20] J. L. Cohn, B. D. White, C. A. M. dos Santos, and J. J. Neumeier, "Giant Nernst effect and bipolarity in the quasi-one-dimensional metal $\text{Li}_{0.9}\text{Mo}_6\text{O}_{17}$," *Phys. Rev. Lett.*, vol. 108, no. 5, pp. 056604/1–056604/5, Feb. 2012.
- [21] S. Z. Butler et al., "Progress, challenges, opportunities in two-dimensional materials beyond graphene," *ACS NANO*, vol. 7, no. 4, pp. 2898–2926, Apr. 2013.
- [22] R. Fei, A. Faghaninia, R. Soklaski, J.-A. Yan, C. Lo, and L. Yang, "Enhanced thermoelectric efficiency via orthogonal electrical and thermal conductances in phosphorene," *Nano Lett.*, vol. 14, no. 11, pp. 6393–6399, Nov. 2014.
- [23] S. A. Wolf, D. D. Awschalom, R. A. Buhrman, J. M. Daughton, S. von Molnár, M. L. Roukes, A. Y. Chtchelkanova, and D. M. Treger, "Spintronics: A spin-based electronics vision for the future," *Science*, vol. 294, no. 5546, pp. 1488–1495, Nov. 2001.
- [24] I. Zutic, J. Fabian, and S. Das Sarma, "Spintronics: Fundamentals and applications," *Rev. Mod. Phys.*, vol. 76, no. 2, pp. 323–410, Apr. 2004.
- [25] G. E. W. Bauer, E. Saitoh, and B. J. van Wees, "Spin caloritronics," *Nature Mater.*, vol. 11, no. 5, pp. 391–399, May 2012.
- [26] K. Uchida, S. Takahashi, K. Harii, J. Ieda, W. Koshibae, K. Ando, S. Maekawa, and E. Saitoh, "Observation of the spin Seebeck effect," *Nature*, vol. 455, no. 7214, pp. 778–781, Oct. 2008.
- [27] S. Maekawa, E. Saitoh, S. O. Valenzuela, and T. Kimura, Eds., *Spin Current*. Oxford, U.K.: Oxford University Press, 2012.
- [28] S. Maekawa, H. Adachi, K. Uchida, J. Ieda, and E. Saitoh, "Spin current: Experimental and theoretical aspects," *J. Phys. Soc. Japan*, vol. 82, no. 10, pp. 102002/1–102002/23, Oct. 2013.
- [29] A. Azevedo, L. H. Vilela-Leao, R. L. Rodríguez-Suárez, A. B. Oliveira, and S. M. Rezende, "dc effect in ferromagnetic resonance: Evidence of the spin-pumping effect?" *J. Appl. Phys.*, vol. 97, no. 10, pp. 10C715/1–10C715/3, May 2005.
- [30] E. Saitoh, M. Ueda, H. Miyajima, and G. Tatara, "Conversion of spin current into charge current at room temperature: Inverse spin-Hall effect," *Appl. Phys. Lett.*, vol. 88, no. 18, pp. 182509/1–182509/3, May 2006.
- [31] S. O. Valenzuela and M. Tinkham, "Direct electronic measurement of the spin Hall effect," *Nature*, vol. 442, no. 7099, pp. 176–179, Jul. 2006.
- [32] M. V. Costache, M. Sladkov, S. M. Watts, C. H. van der Wal, and B. J. van Wees, "Electrical detection of spin pumping due to the precessing magnetization of a single ferromagnet," *Phys. Rev. Lett.*, vol. 97, no. 21, pp. 216603/1–216603/4, Nov. 2006.
- [33] T. Kimura, Y. Otani, T. Sato, S. Takahashi, and S. Maekawa, "Room-temperature reversible spin Hall effect," *Phys. Rev. Lett.*, vol. 98, no. 15, pp. 156601/1–156601/4, Apr. 2007.
- [34] J. Sinova, S. O. Valenzuela, J. Wunderlich, C. H. Back, and T. Jungwirth, "Spin Hall effects," *Rev. Mod. Phys.*, vol. 87, no. 4, pp. 1213–1259, Oct. 2015.
- [35] K. Uchida, T. Ota, K. Harii, K. Ando, H. Nakayama, and E. Saitoh, "Electric detection of the spin-Seebeck effect in ferromagnetic metals," *J. Appl. Phys.*, vol. 107, no. 9, pp. 09A951/1–09A951/5, May 2010.
- [36] S. Bosu, Y. Sakuraba, K. Uchida, K. Saito, T. Ota, E. Saitoh, and K. Takanashi, "Spin Seebeck effect in thin films of the Heusler compound Co_2MnSi ," *Phys. Rev. B*, vol. 83, no. 22, pp. 224401/1–224401/6, Jun. 2011.
- [37] K. Uchida, H. Adachi, T. An, T. Ota, M. Toda, B. Hillebrands, S. Maekawa, and E. Saitoh, "Long-range spin Seebeck effect and acoustic spin pumping," *Nature Mater.*, vol. 10, no. 10, pp. 737–741, Oct. 2011.
- [38] S. H. Wang, L. K. Zou, J. W. Cai, B. G. Shen, and J. R. Sun, "Transverse thermoelectric effects in platinum strips on permalloy films," *Phys. Rev. B*, vol. 88, no. 21, pp. 214304/1–214304/6, Dec. 2013.
- [39] C. M. Jaworski, J. Yang, S. Mack, D. D. Awschalom, J. P. Heremans, and R. C. Myers, "Observation of the spin-Seebeck effect in a ferromagnetic semiconductor," *Nature Mater.*, vol. 9, no. 11, pp. 898–903, Nov. 2010.
- [40] C. M. Jaworski, J. Yang, S. Mack, D. D. Awschalom, R. C. Myers, and J. P. Heremans, "Spin-Seebeck effect: A phonon driven spin distribution," *Phys. Rev. Lett.*, vol. 106, no. 18, pp. 186601/1–186601/4, May 2011.
- [41] K. Uchida et al., "Spin Seebeck insulator," *Nature Mater.*, vol. 9, no. 11, pp. 894–897, Nov. 2010.
- [42] K. Uchida, H. Adachi, T. Ota, H. Nakayama, S. Maekawa, and E. Saitoh, "Observation of longitudinal spin-Seebeck effect in magnetic insulators," *Appl. Phys. Lett.*, vol. 97, no. 17, pp. 172505/1–172505/3, Oct. 2010.
- [43] A. Kirihaara, K. Uchida, Y. Kajiwara, M. Ishida, Y. Nakamura, T. Manako, E. Saitoh, and S. Yorozu, "Spin-current-driven thermoelectric coating," *Nature Mater.*, vol. 11, no. 8, pp. 686–689, Aug. 2012.
- [44] K. Uchida, M. Ishida, T. Kikkawa, A. Kirihaara, T. Murakami, and E. Saitoh, "Longitudinal spin Seebeck effect: From fundamentals to applications," *J. Phys.: Condens. Matter*, vol. 26, no. 34, pp. 343202/1–343202/15, Aug. 2014.
- [45] K. Uchida et al., "Thermal spin pumping and magnon-phonon-mediated spin-Seebeck effect," *J. Appl. Phys.*, vol. 111, no. 10, pp. 103903/1–103903/12, May 2012.
- [46] K. Uchida, T. Nonaka, T. Ota, and E. Saitoh, "Longitudinal spin-Seebeck effect in sintered polycrystalline $(\text{Mn}, \text{Zn})\text{Fe}_2\text{O}_4$," *Appl. Phys. Lett.*, vol. 97, no. 26, pp. 262504/1–262504/3, Dec. 2010.
- [47] K. Uchida, A. Kirihaara, M. Ishida, R. Takahashi, and E. Saitoh, "Local spin-Seebeck effect enabling two-dimensional position sensing," *Japan. J. Appl. Phys.*, vol. 50, no. 12R, pp. 120211/1–120211/3, Dec. 2011.
- [48] M. Weiler et al., "Local charge and spin currents in magnetothermal landscapes," *Phys. Rev. Lett.*, vol. 108, no. 10, pp. 106602/1–106602/5, Mar. 2012.
- [49] K. Uchida, T. Nonaka, T. Yoshino, T. Kikkawa, D. Kikuchi, and E. Saitoh, "Enhancement of spin-Seebeck voltage by spin-Hall thermopile," *Appl. Phys. Exp.*, vol. 5, no. 9, pp. 093001/1–093001/3, Sep. 2012.
- [50] D. Qu, S. Y. Huang, J. Hu, R. Wu, and C. L. Chien, "Intrinsic spin Seebeck effect in Au/YIG ," *Phys. Rev. Lett.*, vol. 110, no. 6, pp. 067206/1–067206/5, Feb. 2013.
- [51] T. Kikkawa, K. Uchida, Y. Shiomi, Z. Qiu, D. Hou, D. Tian, H. Nakayama, X.-F. Jin, and E. Saitoh, "Longitudinal spin Seebeck effect free from the proximity Nernst effect," *Phys. Rev. Lett.*, vol. 110, no. 6, pp. 067207/1–067207/5, Feb. 2013.
- [52] M. B. Jungfleisch et al., "Heat-induced damping modification in yttrium iron garnet/platinum hetero-structures," *Appl. Phys. Lett.*, vol. 102, no. 6, pp. 062417/1–062417/4, Feb. 2013.
- [53] D. Meier et al., "Thermally driven spin and charge currents in thin $\text{NiFe}_2\text{O}_4/\text{Pt}$ films," *Phys. Rev. B*, vol. 87, no. 5, pp. 054421/1–054421/5, Feb. 2013.
- [54] R. Ramos et al., "Observation of the spin Seebeck effect in epitaxial Fe_3O_4 thin films," *Appl. Phys. Lett.*, vol. 102, no. 7, pp. 072413/1–072413/5, Feb. 2013.
- [55] K. Uchida, T. Nonaka, T. Kikkawa, Y. Kajiwara, and E. Saitoh, "Longitudinal spin Seebeck effect in various garnet ferrites," *Phys. Rev. B*, vol. 87, no. 10, pp. 104412/1–104412/6, Mar. 2013.
- [56] B. F. Miao, S. Y. Huang, D. Qu, and C. L. Chien, "Inverse spin Hall effect in a ferromagnetic metal," *Phys. Rev. Lett.*, vol. 111, no. 6, pp. 066602/1–066602/5, Aug. 2013.
- [57] M. Schreier et al., "Magnon, phonon, electron temperature profiles and the spin Seebeck effect in magnetic insulator/normal metal hybrid structures," *Phys. Rev. B*, vol. 88, no. 9, pp. 094410/1–094410/13, Sep. 2013.
- [58] T. Kikkawa et al., "Separation of longitudinal spin Seebeck effect from

- anomalous Nernst effect: Determination of origin of transverse thermoelectric voltage in metal/insulator junctions," *Phys. Rev. B*, vol. 88, no. 21, pp. 214403/1–214403/11, Dec. 2013.
- [59] M. Schreier, N. Roschewsky, E. Dobler, S. Meyer, H. Huebl, R. Gross, and S. T. B. Goennenwein, "Current heating induced spin Seebeck effect," *Appl. Phys. Lett.*, vol. 103, no. 24, pp. 242404/1–242404/4, Dec. 2013.
- [60] S. M. Rezende et al., "Magnon spin-current theory for the longitudinal spin-Seebeck effect," *Phys. Rev. B*, vol. 89, no. 1, pp. 014416/1–014416/10, Jan. 2014.
- [61] A. Azevedo, O. Alves Santos, G. A. Fonseca Guerra, R. O. Cunha, R. Rodriguez-Suárez, and S. M. Rezende, "Competing spin pumping effects in magnetic hybrid structures," *Appl. Phys. Lett.*, vol. 104, no. 5, pp. 052402/1–052402/5, Feb. 2014.
- [62] G. Siegel, M. C. Prestgard, S. Teng, and A. Tiwari, "Robust longitudinal spin-Seebeck effect in Bi-YIG thin films," *Sci. Rep.*, vol. 4, pp. 4429/1–4429/6, Mar. 2014.
- [63] J. B. S. Mendes, R. O. Cunha, O. Alves Santos, P. R. T. Ribeiro, F. L. A. Machado, R. L. Rodríguez-Suárez, A. Azevedo, and S. M. Rezende, "Large inverse spin Hall effect in the antiferromagnetic metal $\text{Ir}_{20}\text{Mn}_{80}$," *Phys. Rev. B*, vol. 89, no. 14, pp. 140406(R)/1–140406(R)/5, Apr. 2014.
- [64] D. Qu, S. Y. Huang, B. F. Miao, S. X. Huang, and C. L. Chien, "Self-consistent determination of spin Hall angles in selected 5d metals by thermal spin injection," *Phys. Rev. B*, vol. 89, no. 14, pp. 140407(R)/1–140407(R)/5, Apr. 2014.
- [65] A. Kehlberger, G. Jakob, M. C. Onbasli, D. H. Kim, C. A. Ross, and M. Kläui, "Investigation of the magnetic properties of insulating thin films using the longitudinal spin Seebeck effect," *J. Appl. Phys.*, vol. 115, no. 17, pp. 17C731/1–17C731/3, May 2014.
- [66] N. Roschewsky et al., "Time resolved spin Seebeck effect experiments," *Appl. Phys. Lett.*, vol. 104, no. 20, pp. 202410/1–202410/4, May 2014.
- [67] M. Agrawal et al., "Role of bulk-magnon transport in the temporal evolution of the longitudinal spin-Seebeck effect," *Phys. Rev. B*, vol. 89, no. 22, pp. 224414/1–224414/5, Jun. 2014.
- [68] M. Agrawal, A. A. Serga, V. Lauer, E. Th. Papaioannou, B. Hillebrands, and V. I. Vasyuchka, "Microwave-induced spin currents in ferromagnetic-insulator |normal metal bilayer system," *Appl. Phys. Lett.*, vol. 105, no. 9, pp. 092404/1–092404/4, Sep. 2014.
- [69] Y. Saiga et al., "Platinum thickness dependence and annealing effect of the spin-Seebeck voltage in platinum/yttrium iron garnet structures," *Appl. Phys. Exp.*, vol. 7, no. 9, pp. 093001/1–093001/4, Sep. 2014.
- [70] S. M. Wu, J. Hoffman, J. E. Pearson, and A. Bhattacharya, "Unambiguous separation of the inverse spin Hall and anomalous Nernst effects within a ferromagnetic metal using the spin Seebeck effect," *Appl. Phys. Lett.*, vol. 105, no. 9, pp. 092409/1–092409/4, Sep. 2014.
- [71] J. Lustikova, Y. Shiomi, Z. Qiu, T. Kikkawa, R. Iguchi, K. Uchida, and E. Saitoh, "Spin current generation from sputtered $\text{Y}_3\text{Fe}_5\text{O}_{12}$ films," *J. Appl. Phys.*, vol. 116, no. 15, pp. 153902/1–153902/6, Oct. 2014.
- [72] A. Aqeel, I. J. Vera-Marun, B. J. van Wees, and T. T. M. Palstra, "Surface sensitivity of the spin Seebeck effect," *J. Appl. Phys.*, vol. 116, no. 15, pp. 153705/1–153705/5, Oct. 2014.
- [73] W. X. Wang, S. H. Wang, L. K. Zou, J. W. Cai, Z. G. Sun, and J. R. Sun, "Joule heating-induced coexisted spin Seebeck effect and spin Hall magnetoresistance in the platinum/ $\text{Y}_3\text{Fe}_5\text{O}_{12}$ structure," *Appl. Phys. Lett.*, vol. 105, no. 18, pp. 182403/1–182403/5, Nov. 2014.
- [74] K. Uchida, T. Kikkawa, A. Miura, J. Shiomi, and E. Saitoh, "Quantitative temperature dependence of longitudinal spin Seebeck effect at high temperatures," *Phys. Rev. X*, vol. 4, no. 4, pp. 041023/1–041023/9, Nov. 2014.
- [75] N. Vlietstra, J. Shan, B. J. van Wees, M. Isasa, F. Casanova, and J. Ben Youssef, "Simultaneous detection of the spin-Hall magnetoresistance and the spin-Seebeck effect in platinum and tantalum on yttrium iron garnet," *Phys. Rev. B*, vol. 90, no. 17, pp. 174436/1–174436/8, Nov. 2014.
- [76] Y. Xu, B. Yang, C. Tang, Z. Jiang, M. Schneider, R. Whig, and J. Shi, "Heat-driven spin transport in a ferromagnetic metal," *Appl. Phys. Lett.*, vol. 105, no. 24, pp. 242404/1–242404/4, Dec. 2014.
- [77] P. Li et al., "Generation of pure spin currents via spin Seebeck effect in self-biased hexagonal ferrite thin films," *Appl. Phys. Lett.*, vol. 105, no. 24, pp. 242412/1–242412/4, Dec. 2014.
- [78] Y. Shiomi and E. Saitoh, "Paramagnetic spin pumping," *Phys. Rev. Lett.*, vol. 113, no. 26, pp. 266602/1–266602/5, Dec. 2014.
- [79] M. Schreier et al., "Sign of inverse spin Hall voltages generated by ferromagnetic resonance and temperature gradients in yttrium iron garnet platinum bilayers," *J. Phys. D: Appl. Phys.*, vol. 48, no. 2, pp. 025001/1–025001/5, Jan. 2015.
- [80] D. Kikuchi, M. Ishida, K. Uchida, Z. Qiu, T. Murakami, and E. Saitoh, "Enhancement of spin-Seebeck effect by inserting ultra-thin $\text{Fe}_{70}\text{Cu}_{30}$ interlayer," *Appl. Phys. Lett.*, vol. 106, no. 8, pp. 082401/1–082401/4, Feb. 2015.
- [81] Z. Qiu, D. Hou, K. Uchida, and E. Saitoh, "Influence of interface condition on spin-Seebeck effects," *J. Phys. D: Appl. Phys.*, vol. 48, no. 16, pp. 164013/1–164013/5, Apr. 2015.
- [82] S. M. Wu, F. Y. Fradin, J. Hoffman, A. Hoffmann, and A. Bhattacharya, "Spin Seebeck devices using local on-chip heating," *J. Appl. Phys.*, vol. 117, pp. 17C509/1–17C509/4, May 2015.
- [83] A. Sola, M. Kuepferling, V. Basso, M. Pasquale, T. Kikkawa, K. Uchida, and E. Saitoh, "Evaluation of thermal gradients in longitudinal spin Seebeck effect measurements," *J. Appl. Phys.*, vol. 117, no. 17, pp. 17C510/1–17C510/4, May 2015.
- [84] H. Asada et al., "Longitudinal spin Seebeck effect in $\text{Nd}_2\text{BiFe}_{5-x}\text{Ga}_x\text{O}_{12}$ prepared on gadolinium gallium garnet (001) by metal organic decomposition method," *J. Appl. Phys.*, vol. 117, no. 17, pp. 17C724/1–17C724/3, May 2015.
- [85] T. Niizeki, T. Kikkawa, K. Uchida, M. Oka, K. Z. Suzuki, H. Yanagihara, E. Kita, and E. Saitoh, "Observation of longitudinal spin-Seebeck effect in cobalt-ferrite epitaxial thin films," *AIP Adv.*, vol. 5, no. 5, pp. 053603/1–053603/6, May 2015.
- [86] S. M. Wu, J. E. Pearson, and A. Bhattacharya, "Paramagnetic spin Seebeck effect," *Phys. Rev. Lett.*, vol. 114, no. 18, pp. 186602/1–186602/5, May 2015.
- [87] D. Tian, Y. Li, D. Qu, X.-F. Jin, and C. L. Chien, "Separation of spin Seebeck effect and anomalous Nernst effect in Co/Cu/YIG," *Appl. Phys. Lett.*, vol. 106, no. 21, pp. 212407/1–212407/4, May 2015.
- [88] K.-D. Lee et al., "Thermoelectric signal enhancement by reconciling the spin Seebeck and anomalous Nernst effects in ferromagnet/non-magnet multilayers," *Sci. Rep.*, vol. 5, pp. 10249/1–10249/10, May 2015.
- [89] Y. Shiomi, Y. Handa, T. Kikkawa, and E. Saitoh, "Transverse thermoelectric effect in $\text{La}_{0.67}\text{Sr}_{0.33}\text{MnO}_3/\text{SrRuO}_3$ superlattices," *Appl. Phys. Lett.*, vol. 106, no. 23, pp. 232403/1–232403/4, Jun. 2015.
- [90] K. Uchida, J. Ohe, T. Kikkawa, S. Daimon, D. Hou, Z. Qiu, and E. Saitoh, "Intrinsic surface magnetic anisotropy in $\text{Y}_3\text{Fe}_5\text{O}_{12}$ as the origin of low-magnetic-field behavior of the spin Seebeck effect," *Phys. Rev. B*, vol. 92, no. 1, pp. 014415/1–014415/8, Jul. 2015.
- [91] D. Qu, S. Y. Huang, and C. L. Chien, "Inverse spin Hall effect in Cr: Independence of antiferromagnetic ordering," *Phys. Rev. B*, vol. 92, no. 2, pp. 020418(R)/1–020418(R)/4, Jul. 2015.
- [92] Z. Qiu, D. Hou, T. Kikkawa, K. Uchida, and E. Saitoh, "All-oxide spin Seebeck effects," *Appl. Phys. Exp.*, vol. 8, no. 8, pp. 083001/1–083001/3, Aug. 2015.
- [93] T. Kikkawa, K. Uchida, S. Daimon, Z. Qiu, Y. Shiomi, and E. Saitoh, "Critical suppression of spin Seebeck effect by magnetic fields," *Phys. Rev. B*, vol. 92, no. 6, pp. 064413/1–064413/9, Aug. 2015.
- [94] H. Jin, S. R. Boona, Z. Yang, R. C. Myers, and J. P. Heremans, "Effect of the magnon dispersion on the longitudinal spin Seebeck effect in yttrium iron garnets," *Phys. Rev. B*, vol. 92, no. 5, pp. 054436/1–054436/8, Aug. 2015.
- [95] A. Kehlberger et al., "Length scale of the spin Seebeck effect," *Phys. Rev. Lett.*, vol. 115, no. 9, pp. 096602/1–096602/5, Aug. 2015.
- [96] T. Seki, K. Uchida, T. Kikkawa, Z. Qiu, E. Saitoh, and K. Takanashi, "Observation of inverse spin Hall effect in ferromagnetic FePt alloys using spin Seebeck effect," *Appl. Phys. Lett.*, vol. 107, no. 9, pp. 092401/1–092401/4, Aug. 2015.
- [97] S. Wang, L. Zou, X. Zhang, J. Cai, S. Wang, B. Shen, and J. Sun, "Spin Seebeck effect and spin Hall magnetoresistance at high temperatures for a Pt/yttrium iron garnet hybrid structure," *Nanoscale*, vol. 7, no. 42, pp. 17812–17819, Nov. 2015.
- [98] U. Ritzmann, D. Hinzke, A. Kehlberger, E.-J. Guo, M. Kläui, and U. Nowak, "Magnetic field control of the spin Seebeck effect," *Phys. Rev. B*, vol. 92, no. 17, pp. 174411/1–174411/5, Nov. 2015.
- [99] A. Aqeel, N. Vlietstra, J. A. Heuvel, G. E. W. Bauer, B. Noheda, B. J. van Wees, and T. T. M. Palstra, "Spin-Hall magnetoresistance and spin Seebeck effect in spin-spiral and paramagnetic phases of multiferroic CoCr_2O_4 films," *Phys. Rev. B*, vol. 92, no. 22, pp. 224410/1–224410/8, Dec. 2015.

- [100] R. Ramos et al., "Unconventional scaling and significant enhancement of the spin Seebeck effect in multilayers," *Phys. Rev. B*, vol. 92, no. 22, pp. 220407(R)/1–220407(R)/5, Dec. 2015.
- [101] A. Kiriha et al., "Spin-Seebeck thermoelectric converter," in *Proc. IEEE Int. Nanoelectron. Conf.*, pp. 1–3, Jul. 28–31, 2014.
- [102] S. Geprägs et al., "Origin of the spin Seebeck effect in compensated ferrimagnets," *Nature Commun.*, vol. 7, pp. 10452/1–10452/6, Feb. 2016.
- [103] E.-J. Guo, A. Kehlberger, J. Cramer, G. Jakob, and M. Kläui, "Origin of the thickness-dependent low-temperature enhancement of spin Seebeck effect in YIG films," 2015. [Online]. Available: <http://arxiv.org/abs/1506.06037>.
- [104] S. Seki et al., "Thermal generation of spin current in an antiferromagnet," *Phys. Rev. Lett.*, vol. 115, no. 26, pp. 266601/1–266601/5, Dec. 2015.
- [105] S. M. Wu et al., "Antiferromagnetic spin Seebeck effect," *Phys. Rev. Lett.*, vol. 116, no. 9, pp. 097204/1–097204/5, Mar. 2016.
- [106] A. Kiriha et al., "Flexible heat-flow sensing sheets based on the longitudinal spin Seebeck effect using one-dimensional spin-current conducting films," *Sci. Rep.*, vol. 6, pp. 23114/1–23114/7, Mar. 2016.
- [107] E.-J. Guo, A. Herklotz, A. Kehlberger, J. Cramer, G. Jakob, and M. Kläui, "Thermal generation of spin current in epitaxial CoFe_2O_4 thin films," *Appl. Phys. Lett.*, vol. 108, no. 2, pp. 022403/1–022403/5, Jan. 2016.
- [108] L. K. Zou, S. H. Wang, Y. Zhang, J. R. Sun, J. W. Cai, and S. S. Kang, "Large extrinsic spin Hall effect in Au-Cu alloys by extensive atomic disorder scattering," *Phys. Rev. B*, vol. 93, no. 1, pp. 014422/1–014422/6, Jan. 2016.
- [109] B. F. Miao, S. Y. Huang, D. Qu, and C. L. Chien, "Absence of anomalous Nernst effect in spin Seebeck effect of Pt/YIG," *AIP Adv.*, vol. 6, no. 1, pp. 015018/1–015018/6, Jan. 2016.
- [110] R. Takagi, Y. Tokunaga, T. Ideue, Y. Taguchi, Y. Tokura, and S. Seki, "Thermal generation of spin current in a multiferroic helimagnet," *APL Mater.*, vol. 4, no. 3, pp. 032502/1–032502/7, Mar. 2016.
- [111] S. Y. Huang, W. G. Wang, S. F. Lee, J. Kwo, and C. L. Chien, "Intrinsic spin-dependent thermal transport," *Phys. Rev. Lett.*, vol. 107, no. 21, pp. 216604/1–216604/4, Nov. 2011.
- [112] S. Bosu, Y. Sakuraba, K. Uchida, K. Saito, W. Kobayashi, E. Saitoh, and K. Takanashi, "Thermal artifact on the spin Seebeck effect in metallic thin films deposited on MgO substrates," *J. Appl. Phys.*, vol. 111, no. 7, pp. 07B106/1–07B106/3, Apr. 2012.
- [113] D. Meier et al., "Longitudinal spin Seebeck effect contribution in transverse spin Seebeck effect experiments in Pt/YIG and Pt/NFO," *Nature Commun.*, vol. 6, pp. 8211/1–8211/7, Sep. 2015.
- [114] W.-L. Lee, S. Watauchi, V. L. Miller, R. J. Cava, and N. P. Ong, "Anomalous Hall heat current and Nernst effect in the $\text{CuCr}_2\text{Se}_4\text{-xBr}_x$ ferromagnet," *Phys. Rev. Lett.*, vol. 93, no. 22, pp. 226601/1–226601/4, Nov. 2004.
- [115] T. Miyasato et al., "Crossover behavior of the anomalous Hall effect and anomalous Nernst effect in itinerant ferromagnets," *Phys. Rev. Lett.*, vol. 99, no. 8, pp. 086602/1–086602/4, Aug. 2007.
- [116] Y. Pu, D. Chiba, F. Matsukura, H. Ohno, and J. Shi, "Mott relation for anomalous Hall and Nernst effects in $\text{Ga}_{1-x}\text{Mn}_x\text{As}$ ferromagnetic semiconductors," *Phys. Rev. Lett.*, vol. 101, no. 11, pp. 117208/1–117208/4, Sep. 2008.
- [117] M. Mizuguchi, S. Ohata, K. Uchida, E. Saitoh, and K. Takanashi, "Anomalous Nernst effect in an LiO -ordered epitaxial FePt thin film," *Appl. Phys. Exp.*, vol. 5, no. 9, pp. 093002/1–093002/3, Sep. 2012.
- [118] Y. Sakuraba, K. Hasegawa, M. Mizuguchi, T. Kubota, S. Mizukami, T. Miyazaki, and K. Takanashi, "Anomalous Nernst effect in LiO -FePt/MnGa thermopiles for new thermoelectric applications," *Appl. Phys. Exp.*, vol. 6, no. 3, pp. 033003/1–033003/4, Mar. 2013.
- [119] R. Ramos et al., "Anomalous Nernst effect of Fe_3O_4 single crystal," *Phys. Rev. B*, vol. 90, no. 5, pp. 054422/1–054422/6, Aug. 2014.
- [120] K. Uchida, T. Kikkawa, T. Seki, T. Oyake, J. Shiomi, Z. Qiu, K. Takanashi, and E. Saitoh, "Enhancement of anomalous Nernst effects in metallic multilayers free from proximity-induced magnetism," *Phys. Rev. B*, vol. 92, no. 9, pp. 094414/1–094414/6, Sep. 2015.
- [121] Y. Sakuraba, "Potential of thermoelectric power generation using anomalous Nernst effect in magnetic materials," *Scripta Mater.*, vol. 111, pp. 29–32, Jan. 2016.
- [122] A. D. Avery, M. R. Pufall, and B. L. Zink, "Observation of the planar Nernst effect in permalloy and nickel thin films with in-plane thermal gradients," *Phys. Rev. Lett.*, vol. 109, no. 19, pp. 196602/1–196602/5, Nov. 2012.
- [123] M. Schmid et al., "Transverse spin Seebeck effect versus anomalous and planar Nernst effects in permalloy thin films," *Phys. Rev. Lett.*, vol. 111, no. 18, pp. 187201/1–187201/5, Oct. 2013.
- [124] D. Meier, D. Reinhardt, M. Schmid, C. H. Back, J.-M. Schmalhorst, T. Kuschel, and G. Reiss, "Influence of heat flow directions on Nernst effects in Py/Pt bilayers," *Phys. Rev. B*, vol. 88, no. 18, pp. 184425/1–184425/6, Nov. 2013.
- [125] I. V. Soldatov, N. Panarina, C. Hess, L. Schultz, and R. Schäfer, "Thermoelectric effects and magnetic anisotropy of $\text{Ga}_{1-x}\text{Mn}_x\text{As}$ thin films," *Phys. Rev. B*, vol. 90, no. 10, pp. 104423/1–104423/9, Sep. 2014.
- [126] L. J. Cornelissen, J. Liu, R. A. Duine, J. Ben Youssef, and B. J. van Wees, "Long-distance transport of magnon spin information in a magnetic insulator at room temperature," *Nature Phys.*, vol. 11, no. 12, pp. 1022–1026, Dec. 2015.
- [127] S. T. B. Goennenwein, R. Schlitz, M. Pernpeintner, K. Ganzhorn, M. Althammer, R. Gross, and H. Huebl, "Non-local magnetoresistance in YIG/Pt nanostructures," *Appl. Phys. Lett.*, vol. 107, no. 17, pp. 172405/1–172405/4, Oct. 2015.
- [128] B. L. Giles, Z. Yang, J. Jamison, and R. C. Myers, "Long-range pure magnon spin diffusion observed in a nonlocal spin-Seebeck geometry," *Phys. Rev. B*, vol. 92, no. 22, pp. 224415/1–224415/13, Dec. 2015.
- [129] L. J. Cornelissen and B. J. van Wees, "Magnetic field dependence of the magnon spin diffusion length in the magnetic insulator yttrium iron garnet," *Phys. Rev. B*, vol. 93, no. 2, pp. 020403(R)/1–020403(R)/5, Jan. 2016.
- [130] A. B. Cahaya, O. A. Tretiakov, and G. E. W. Bauer, "Spin Seebeck power generators," *Appl. Phys. Lett.*, vol. 104, no. 4, pp. 042402/1–042402/4, Jan. 2014.
- [131] T. Liao, J. Lin, G. Su, B. Lin, and J. Chen, "Optimum design of a nanoscale spin-Seebeck power device," *Nanoscale*, vol. 7, no. 17, pp. 7920–7926, May 2015.
- [132] A. B. Cahaya, O. A. Tretiakov, and G. E. W. Bauer, "Spin Seebeck power conversion," *IEEE Trans. Magn.*, vol. 51, no. 9, pp. 0800414/1–0800414/14, Sep. 2015.
- [133] Y. Tserkovnyak, A. Brataas, G. E. W. Bauer, and B. I. Halperin, "Nonlocal magnetization dynamics in ferromagnetic heterostructures," *Rev. Mod. Phys.*, vol. 77, no. 4, pp. 1375–1421, Dec. 2005.
- [134] X. Jia, K. Liu, K. Xia, and G. E. W. Bauer, "Spin transfer torque on magnetic insulators," *Europhys. Lett.*, vol. 96, no. 1, pp. 17005/1–17005/6, Oct. 2011.
- [135] M. Weiler et al., "Experimental test of the spin mixing interface conductivity concept," *Phys. Rev. Lett.*, vol. 111, no. 17, pp. 176601/1–176601/5, Oct. 2013.
- [136] Y. Ohnuma, H. Adachi, E. Saitoh, and S. Maekawa, "Enhanced dc spin pumping into a fluctuating ferromagnet near T_C ," *Phys. Rev. B*, vol. 89, no. 17, pp. 174417/1–174417/10, May 2014.
- [137] H. Jiao and G. E. W. Bauer, "Spin backflow and ac voltage generation by spin pumping and the inverse spin Hall effect," *Phys. Rev. Lett.*, vol. 110, no. 21, pp. 217602/1–217602/5, May 2013.
- [138] M. B. Jungfleisch, V. Lauer, R. Neb, A. V. Chumak, and B. Hillebrands, "Improvement of the yttrium iron garnet/platinum interface for spin pumping-based applications," *Appl. Phys. Lett.*, vol. 103, no. 2, pp. 022411/1–022411/4, Jul. 2013.
- [139] Z. Qiu, K. Ando, K. Uchida, Y. Kajiwara, R. Takahashi, H. Nakayama, T. An, Y. Fujikawa, and E. Saitoh, "Spin mixing conductance at a well-controlled platinum/yttrium iron garnet interface," *Appl. Phys. Lett.*, vol. 103, no. 9, pp. 092404/1–092404/4, Aug. 2013.
- [140] M. Morota, Y. Niimi, K. Ohnishi, D. H. Wei, T. Tanaka, H. Kontani, T. Kimura, and Y. Otani, "Indication of intrinsic spin Hall effect in 4d and 5d transition metals," *Phys. Rev. B*, vol. 83, no. 17, pp. 174405/1–174405/5, May 2011.
- [141] H. L. Wang, C. H. Du, Y. Pu, R. Adur, P. C. Hammel, and F. Y. Yang, "Scaling of spin Hall angle in 3d, 4d, and 5d metals from $\text{Y}_3\text{Fe}_5\text{O}_{12}$ /metal spin pumping," *Phys. Rev. Lett.*, vol. 112, no. 19, pp. 197201/1–197201/5, May 2014.
- [142] S. Singh, M. Anguerra, E. del Barco, R. Springell, and C. W. Miller, "Moderate positive spin Hall angle in uranium," *Appl. Phys. Lett.*, vol. 107, no. 23, pp. 232403/1–232403/5, Dec. 2015.
- [143] Y. Niimi et al., "Extrinsic spin Hall effect induced by iridium impurities in copper," *Phys. Rev. Lett.*, vol. 106, no. 12, pp. 126601/1–126601/4, Mar. 2011.
- [144] Y. Niimi et al., "Giant spin Hall effect induced by skew scattering from bismuth impurities inside thin film CuBi alloys," *Phys. Rev. Lett.*, vol. 109, no. 15, pp. 156602/1–156602/5, Oct. 2012.
- [145] P. Laczowski et al., "Experimental evidences of a large extrinsic spin Hall effect in AuW alloy," *Appl. Phys. Lett.*, vol. 104, no. 14, pp. 142403/1–142403/5, Apr. 2014.

- [146] K. Ando et al., "Electrically tunable spin injector free from the impedance mismatch problem," *Nature Mater.*, vol. 10, no. 9, pp. 655–659, Sep. 2011.
- [147] L. Chen, F. Matsukura, and H. Ohno, "Direct-current voltages in (Ga,Mn)As structures induced by ferromagnetic resonance," *Nature Commun.*, vol. 4, pp. 2055/1–2055/6, Jun. 2013.
- [148] J.-C. Rojas-Sánchez et al., "Spin pumping and inverse spin Hall effect in germanium," *Phys. Rev. B*, vol. 88, no. 6, pp. 064403/1–064403/15, Aug. 2013.
- [149] J.-C. Lee, L.-W. Huang, D.-S. Hung, T.-H. Chiang, J. C. A. Huang, J.-Z. Liang, and S.-F. Lee, "Inverse spin Hall effect induced by spin pumping into semiconducting ZnO," *Appl. Phys. Lett.*, vol. 104, no. 5, pp. 052401/1–052401/4, Feb. 2014.
- [150] Z. Qiu et al., "All-oxide system for spin pumping," *Appl. Phys. Lett.*, vol. 100, no. 2, pp. 022402/1–022402/3, Jan. 2012.
- [151] K. Fujiwara, Y. Fukuma, J. Matsuno, H. Idzuchi, Y. Niimi, Y. Otani, and H. Takagi, "5d iridium oxide as a material for spin-current detection," *Nature Commun.*, vol. 4, pp. 2893/1–2893/6, Dec. 2013.
- [152] K. Ando, S. Watanabe, S. Mooser, E. Saitoh, and H. Siringhaus, "Solution-processed organic spin-charge converter," *Nature Mater.*, vol. 12, no. 7, pp. 622–627, Jul. 2013.
- [153] Z. Qiu, M. Uruichi, D. Hou, K. Uchida, H. M. Yamamoto, and E. Saitoh, "Spin-current injection and detection in $\kappa - (\text{BEDT-TTF})_2\text{Cu}[\text{N}(\text{CN})_2]\text{Br}$," *AIP Adv.*, vol. 5, no. 5, pp. 057167/1–057167/7, May 2015.
- [154] R. H. Silsbee, A. Janossy, and P. Monod, "Coupling between ferromagnetic and conduction-spin-resonance modes at a ferromagnetic–normal-metal interface," *Phys. Rev. B*, vol. 19, no. 9, pp. 4382–4399, May 1979.
- [155] Y. Tserkovnyak, A. Brataas, and G. E. W. Bauer, "Enhanced Gilbert damping in thin ferromagnetic films," *Phys. Rev. Lett.*, vol. 88, no. 11, pp. 117601/1–117601/4, Feb. 2002.
- [156] S. Mizukami, Y. Ando, and T. Miyazaki, "Effect of spin diffusion on Gilbert damping for a very thin permalloy layer in Cu/permalloy/Cu/Pt films," *Phys. Rev. B*, vol. 66, no. 10, pp. 104413/1–104413/9, Sep. 2002.
- [157] Y. Kajiwara et al., "Transmission of electrical signals by spin-wave interconversion in a magnetic insulator," *Nature*, vol. 464, no. 7286, pp. 262–266, Mar. 2010.
- [158] Y.-T. Chen, S. Takahashi, H. Nakayama, M. Althammer, S. T. B. Goennenwein, E. Saitoh, and G. E. W. Bauer, "Theory of spin Hall magnetoresistance," *Phys. Rev. B*, vol. 87, no. 14, pp. 144411/1–144411/9, Apr. 2013.
- [159] H. Nakayama et al., "Spin Hall magnetoresistance induced by a nonequilibrium proximity effect," *Phys. Rev. Lett.*, vol. 110, no. 20, pp. 206601/1–206601/5, May 2013.
- [160] C. Hahn, G. de Loubens, O. Klein, M. Viret, V. V. Naletov, and J. Ben Youssef, "Comparative measurements of inverse spin Hall effects and magnetoresistance in YIG/Pt and YIG/Ta," *Phys. Rev. B*, vol. 87, no. 17, pp. 174417/1–174417/8, May 2013.
- [161] N. Vlietstra, J. Shan, V. Castel, J. Ben Youssef, and B. J. van Wees, "Spin-Hall magnetoresistance in platinum on yttrium iron garnet: Dependence on platinum thickness and in-plane/out-of-plane magnetization," *Phys. Rev. B*, vol. 87, no. 18, pp. 184421/1–184421/5, May 2013.
- [162] M. Althammer et al., "Quantitative study of the spin Hall magnetoresistance in ferromagnetic insulator/normal metal hybrids," *Phys. Rev. B*, vol. 87, no. 22, pp. 224401/1–224401/15, Jun. 2013.
- [163] F. J. Jedema, A. T. Filip, and B. J. van Wees, "Electrical spin injection and accumulation at room temperature in an all-metal mesoscopic spin valve," *Nature*, vol. 410, no. 6826, pp. 345–348, Mar. 2001.
- [164] F. J. Jedema, H. B. Heersche, A. T. Filip, J. J. A. Baselmans, and B. J. van Wees, "Electrical detection of spin precession in a metallic mesoscopic spin valve," *Nature*, vol. 416, no. 6882, pp. 713–716, Apr. 2002.
- [165] Y. Niimi and Y. Otani, "Reciprocal spin Hall effects in conductors with strong spin-orbit coupling: A review," *Rep. Prog. Phys.*, vol. 78, no. 12, pp. 124501/1–124501/19, Dec. 2015.
- [166] J. Xiao, G. E. W. Bauer, K. Uchida, E. Saitoh, and S. Maekawa, "Theory of magnon-driven spin Seebeck effect," *Phys. Rev. B*, vol. 81, no. 21, pp. 214418/1–214418/8, Jun. 2010.
- [167] H. Adachi, K. Uchida, E. Saitoh, J. Ohe, S. Takahashi, and S. Maekawa, "Gigantic enhancement of spin Seebeck effect by phonon drag," *Appl. Phys. Lett.*, vol. 97, no. 25, pp. 252506/1–252506/3, Dec. 2010.
- [168] H. Adachi, J. Ohe, S. Takahashi, and S. Maekawa, "Linear-response theory of spin Seebeck effect in ferromagnetic insulators," *Phys. Rev. B*, vol. 83, no. 9, pp. 094410/1–094410/6, Mar. 2011.
- [169] J. Ohe, H. Adachi, S. Takahashi, and S. Maekawa, "Numerical study on the spin Seebeck effect," *Phys. Rev. B*, vol. 83, no. 11, pp. 115118/1–115118/5, Mar. 2011.
- [170] S. A. Bender, R. A. Duine, and Y. Tserkovnyak, "Electronic pumping of quasiequilibrium Bose-Einstein-condensed magnons," *Phys. Rev. Lett.*, vol. 108, no. 24, pp. 246601/1–246601/5, Jun. 2012.
- [171] Y. Ohnuma, H. Adachi, E. Saitoh, and S. Maekawa, "Spin Seebeck effect in antiferromagnets and compensated ferrimagnets," *Phys. Rev. B*, vol. 87, no. 1, pp. 014423/1–014423/7, Jan. 2013.
- [172] H. Adachi, K. Uchida, E. Saitoh, and S. Maekawa, "Theory of the spin Seebeck effect," *Rep. Prog. Phys.*, vol. 76, no. 3, pp. 036501/1–036501/20, Mar. 2013.
- [173] S. Hoffman, K. Sato, and Y. Tserkovnyak, "Landau-Lifshitz theory of the longitudinal spin Seebeck effect," *Phys. Rev. B*, vol. 88, no. 6, pp. 064408/1–064408/8, Aug. 2013.
- [174] L. Chotorlishvili, Z. Toklikishvili, V. K. Dugaev, J. Barnaś, S. Trimper, and J. Berakdar, "Fokker-Planck approach to the theory of the magnon-driven spin Seebeck effect," *Phys. Rev. B*, vol. 88, no. 14, pp. 144429/1–144429/6, Oct. 2013.
- [175] J. Ren, "Predicted rectification and negative differential spin Seebeck effect at magnetic interfaces," *Phys. Rev. B*, vol. 88, no. 22, pp. 220406(R)/1–220406(R)/5, Dec. 2013.
- [176] S. A. Bender and Y. Tserkovnyak, "Interfacial spin and heat transfer between metals and magnetic insulators," *Phys. Rev. B*, vol. 91, no. 14, pp. 140402(R)/1–140402(R)/5, Apr. 2015.
- [177] I. I. Lyapilin, M. S. Okorokov, and V. V. Ustinov, "Spin effects induced by thermal perturbation in a normal metal/magnetic insulator system," *Phys. Rev. B*, vol. 91, no. 19, pp. 195309/1–195309/7, May 2015.
- [178] S. R. Etesami, L. Chotorlishvili, and J. Berakdar, "Spectral characteristics of time resolved magnonic spin Seebeck effect," *Appl. Phys. Lett.*, vol. 107, no. 13, pp. 132402/1–132402/4, Sep. 2015.
- [179] A. Brataas, H. Skarsvåg, E. G. Tveten, and E. L. Fjærhu, "Heat transport between antiferromagnetic insulators and normal metals," *Phys. Rev. B*, vol. 92, no. 18, pp. 180414(R)/1–180414(R)/5, Nov. 2015.
- [180] L. Chotorlishvili, Z. Toklikishvili, S. R. Etesami, V. K. Dugaev, J. Barnaś, and J. Berakdar, "Magnon-driven longitudinal spin Seebeck effect in F/N and N/F/N structures: Role of asymmetric in-plane magnetic anisotropy," *J. Magn. Magn. Mater.*, vol. 396, pp. 254–262, Dec. 2015.
- [181] S. M. Rezende, R. L. Rodríguez-Suárez, and A. Azevedo, "Theory of the spin Seebeck effect in antiferromagnets," *Phys. Rev. B*, vol. 93, no. 1, pp. 014425/1–014425/9, Jan. 2016.
- [182] J. Xiao and G. E. W. Bauer, "Transport between metals and magnetic insulators," 2015. [Online]. Available: <http://arxiv.org/abs/1508.02486>.
- [183] S. Y. Huang et al., "Transport magnetic proximity effects in platinum," *Phys. Rev. Lett.*, vol. 109, no. 10, pp. 107204/1–107204/5, Sep. 2012.
- [184] S. Geprägs et al., "Investigation of induced Pt magnetic polarization in Pt/Y₃Fe₅O₁₂ bilayers," *Appl. Phys. Lett.*, vol. 101, no. 26, pp. 262407/1–262407/4, Dec. 2012.
- [185] Y. M. Lu et al., "Pt magnetic polarization on Y₃Fe₅O₁₂ and magnetotransport characteristics," *Phys. Rev. Lett.*, vol. 110, no. 14, pp. 147207/1–147207/5, Apr. 2013.
- [186] S. Geprägs et al., "Comment on 'Pt magnetic polarization on Y₃Fe₅O₁₂ and magnetotransport characteristics,'" 2013. [Online]. Available: <http://arxiv.org/abs/1307.4869>.
- [187] Y. Sun et al., "Damping in yttrium iron garnet nanoscale films capped by platinum," *Phys. Rev. Lett.*, vol. 111, no. 10, pp. 106601/1–106601/5, Sep. 2013.
- [188] B. F. Miao, S. Y. Huang, D. Qu, and C. L. Chien, "Physical origins of the new magnetoresistance in Pt/YIG," *Phys. Rev. Lett.*, vol. 112, no. 23, pp. 236601/1–236601/5, Jun. 2014.
- [189] G. Y. Guo, Q. Niu, and N. Nagaosa, "Anomalous Nernst and Hall effects in magnetized platinum and palladium," *Phys. Rev. B*, vol. 89, no. 21, pp. 214406/1–214406/6, Jun. 2014.
- [190] M. Haertinger et al., "Spin pumping in YIG/Pt bilayers as a function of layer thickness," *Phys. Rev. B*, vol. 92, no. 5, pp. 054437/1–054437/6, Aug. 2015.
- [191] D. A. Papaconstantopoulos, *Handbook of the Band Structure of Elemental Solids*. New York, NY, USA: Plenum Press, 1986.
- [192] H. Ibach and H. Lüth, *Solid-State Physics: An Introduction to Principles of Materials Science*. Berlin, Germany: Springer-Verlag, 2009.
- [193] S. M. Rezende, R. L. Rodríguez-Suárez, R. O. Cunha, J. C. López Ortiz, and A. Azevedo, "Bulk magnon spin current theory for the longitudinal spin Seebeck

- effect," *J. Magn. Magn. Mater.*, vol. 400, pp. 171–177, Feb. 2016.
- [194] D. J. Sanders and D. Walton, "Effect of magnon-phonon thermal relaxation on heat transport by magnons," *Phys. Rev. B*, vol. 15, no. 3, pp. 1489–1494, Feb. 1977.
- [195] S. S.-L. Zhang and S. Zhang, "Magnon mediated electric current drag across a ferromagnetic insulator layer," *Phys. Rev. Lett.*, vol. 109, no. 9, pp. 096603/1–096603/5, Aug. 2012.
- [196] S. S.-L. Zhang and S. Zhang, "Spin convection at magnetic interfaces," *Phys. Rev. B*, vol. 86, no. 21, pp. 214424/1–214424/7, Dec. 2012.
- [197] M. Agrawal, V. I. Vasyuchka, A. A. Serga, A. D. Karenowska, G. A. Melkov, and B. Hillebrands, "Direct measurement of magnon temperature: New insight into magnon-phonon coupling in magnetic insulators," *Phys. Rev. Lett.*, vol. 111, no. 10, pp. 107204/1–107204/5, Sep. 2013.
- [198] A. Rückriegel, P. Kopietz, D. A. Bozhko, A. A. Serga, and B. Hillebrands, "Magnetoelastic modes and lifetime of magnons in thin yttrium iron garnet films," *Phys. Rev. B*, vol. 89, no. 18, pp. 184413/1–184413/14, May 2014.
- [199] S. R. Boona and J. P. Heremans, "Magnon thermal mean free path in yttrium iron garnet," *Phys. Rev. B*, vol. 90, no. 6, pp. 064421/1–064421/8, Aug. 2014.
- [200] T. C. Harman and J. M. Honig, "Theory of galvano-thermoelectric energy conversion devices. I. Generators," *J. Appl. Phys.*, vol. 33, no. 11, pp. 3178–3188, Nov. 1962.
- [201] T. C. Harman and J. M. Honig, "Theory of galvano-thermoelectric energy conversion devices. II. Refrigerators and heat pumps," *J. Appl. Phys.*, vol. 33, no. 11, pp. 3188–3194, Nov. 1962.
- [202] T. C. Harman and J. M. Honig, "Theory of galvano-thermoelectric energy conversion devices. III. Generators constructed from anisotropic materials," *J. Appl. Phys.*, vol. 34, no. 1, pp. 189–194, Nov. 1963.
- [203] L. D. Landau, E. M. Lifshitz, and L. P. Pitaevskii, *Electrodynamics of Continuous Media*. Oxford, U.K.: Pergamon Press, 1984.
- [204] Y. Zhang, N. P. Ong, Z. A. Xu, K. Krishana, R. Gagnon, and L. Taillefer, "Determining the Wiedemann-Franz ratio from the thermal Hall conductivity: Application to Cu and YBa₂Cu₃O_{6.95}," *Phys. Rev. Lett.*, vol. 84, no. 10, pp. 2219–2222, Mar. 2000.
- [205] Y. Shiomi, Y. Onose, and Y. Tokura, "Effect of scattering on intrinsic anomalous Hall effect investigated by Lorenz ratio," *Phys. Rev. B*, vol. 81, no. 5, pp. 054414/1–054414/6, Feb. 2010.
- [206] W. M. Yim and A. Amith, "Bi-Sb alloys for magneto-thermoelectric and thermomagnetic cooling," *Solid-State Electron.*, vol. 15, no. 10, pp. 1141–1165, Oct. 1972.
- [207] C. A. Domenicali, "Stationary temperature distribution in an electrically heated conductor," *J. Appl. Phys.*, vol. 25, no. 10, pp. 1310–1311, Oct. 1954.
- [208] R. R. Heikes and R. W. Ure, Jr., *Thermoelectricity: Science and Engineering*. New York, NY, USA: Interscience Publishers Inc., 1961.
- [209] G. D. Mahan, "Good Thermoelectrics," *Solid State Phys.*, vol. 51, pp. 81–157, Sep. 1997.
- [210] R. B. Horst, "Thermomagnetic figure of merit: Bismuth," *J. Appl. Phys.*, vol. 34, no. 11, pp. 3246–3254, Nov. 1963.
- [211] R. T. Delves, "Figure of merit for Ettingshausen cooling," *Brit. J. Appl. Phys.*, vol. 15, no. 1, pp. 105–106, Jan. 1964.
- [212] J. Flipse, F. K. Dejene, D. Wagenaar, G. E. W. Bauer, J. Ben Youssef, and B. J. van Wees, "Observation of the spin Peltier effect for magnetic insulators," *Phys. Rev. Lett.*, vol. 113, no. 2, pp. 027601/1–027601/5, Jul. 2014.
- [213] A. A. Tulapurkar and Y. Suzuki, "Boltzmann approach to dissipation produced by a spin-polarized current," *Phys. Rev. B*, vol. 83, no. 1, pp. 012401/1–012401/4, Jan. 2011.
- [214] M. Abe, T. Itoh, and Y. Tamaura, "Magnetic and biomagnetic films obtained by ferrite plating in aqueous solution," *Thin Solid Films*, vol. 216, no. 1, pp. 155–161, Aug. 1992.
- [215] K. Kondo, S. Yoshida, H. Ono, and M. Abe, "Spin sprayed Ni(-Zn)-Co ferrite films with natural resonance frequency exceeding 3 GHz," *J. Appl. Phys.*, vol. 101, no. 9, pp. 09M502/1–09M502/3, May 2007.
- [216] A. Slachter, F. L. Bakker, J.-P. Adam, and B. J. van Wees, "Thermally driven spin injection from a ferromagnet into a non-magnetic metal," *Nature Phys.*, vol. 6, no. 11, pp. 879–882, Nov. 2010.
- [217] J.-C. Le Breton, S. Sharma, H. Saito, S. Yuasa, and R. Jansen, "Thermal spin current from a ferromagnet to silicon by Seebeck spin tunnelling," *Nature*, vol. 475, no. 7354, pp. 82–85, Jul. 2011.
- [218] M. Walter et al., "Seebeck effect in magnetic tunnel junctions," *Nature Mater.*, vol. 10, no. 10, pp. 742–746, Oct. 2011.
- [219] M. V. Costache, G. Bridoux, I. Neumann, and S. O. Valenzuela, "Magnon-drag thermopile," *Nature Mater.*, vol. 11, no. 3, pp. 199–202, Mar. 2012.
- [220] C. M. Jaworski, R. C. Myers, E. Johnston-Halperin, and J. P. Heremans, "Giant spin Seebeck effect in a non-magnetic material," *Nature*, vol. 487, no. 7406, pp. 210–213, Jul. 2012.

ABOUT THE AUTHORS

Ken-ichi Uchida was born in Kanagawa Prefecture, Japan, in 1986. He received the B.Eng. and M.Sc.Eng. degrees from Keio University, Yokohama, Japan, in 2008 and 2009, respectively, and the Ph.D. degree from Tohoku University, Sendai, Japan, in 2012.

He was an Assistant Professor at the Institute for Materials Research, Tohoku University from 2012 to 2014. He has been an Associate Professor at the Institute for Materials Research, Tohoku University, since 2014, and a PRESTO Researcher at Japan Science and Technology Agency, since 2012. He has worked on spintronics and spin caloritronics. He has developed thermal, acoustic, and plasmonic methods of generating spin currents and realized thermoelectric generation using insulators.



Hiroto Adachi was born in Aichi Prefecture, Japan, in 1975. He received the B.Sc., M.Sc., and D.Sc. degrees from Kyoto University, Kyoto, Japan, in 1998, 2000, and 2003, respectively.

He was a Postdoctoral Research Assistant at Okayama University, Okayama, Japan, from 2003 to 2007, at the Swiss Federal Institute of Technology (ETH) Zurich, Zurich, Switzerland, from 2007 to 2009, at the Institute for Materials Research, Tohoku University, Sendai, Japan, from 2009 to 2010, and at the Advanced Science Research Center, Japan Atomic Energy Agency, Tokai, Japan, from 2010 to 2011. Since 2011, he



has been a Senior PD Fellow at the Advanced Science Research Center, Japan Atomic Energy Agency. His research interests include spintronics and superconductivity.

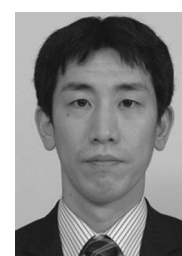
Takashi Kikkawa was born in Kanagawa Prefecture, Japan, in 1991. He received the B.Sc. and M.Sc. degrees from Tohoku University, Sendai, Japan, in 2013 and 2015, respectively. He is currently working toward the Ph.D. degree in science at Tohoku University.

Since 2015, he has been supported by the Japan Society for the Promotion of Science through a research fellowship for young scientists. His research interest includes the investigation of thermo-spin effects in magnetic materials.



Akihiro Kirihiro was born in Saga Prefecture, Japan, in 1979. He received the B.Eng. and M.Eng. degrees from the University of Tokyo, Tokyo, Japan, in 2002 and 2004, respectively.

He has belonged to NEC Corporation since 2004. He was a Visiting Researcher at Technische Universität Kaiserslautern, Kaiserslautern, Germany, from 2013 to 2014. Since 2014, he has also been a Research Member of the ERATO "Spin Quantum Rectification" project at Japan Science and Technology Agency. His research interests include spintronics, spin caloritronics, and thermoelectric conversion devices.



Masahiko Ishida was born in Fukushima Prefecture, Japan, in 1972. He received the B.Eng., M.Eng., and D.Eng. degrees from University of Tsukuba, Tsukuba, Japan, in 1995, 1997, and 1999, respectively.

After spending one year of postdoctoral research at University of Tsukuba, he joined Fundamental Research Laboratories, NEC Corporation in 2000. He was also a Visiting Researcher at the California Nanosystems Institute, University of California, Los Angeles, California, USA, from 2007 to 2008. Since 2014, he has been leading the Spin Thermoelectrics Team at Smart Energy Research Laboratories, NEC Corporation, and the spin Seebeck effect utilization group of the ERATO "Spin Quantum Rectification" project at Japan Science and Technology Agency. He has worked on various fields of electronic and sensing device fabrication.



Shinichi Yorozu was born in Ibaraki Prefecture, Japan, in 1965. He received the B.Eng. degree from Hokkaido University, Hokkaido, Japan, in 1988, and the M.Eng. and Ph.D. degrees from the University of Tokyo, Tokyo, Japan, in 1990 and 1993, respectively.

He joined Fundamental Research Laboratories, NEC Corporation in 1993. He was a Visiting Researcher at the State University of New York at Stony Brook, New York, USA, from 1997 to 1998. He was a Senior Manager of the Fundamental and Environmental Research Laboratories, NEC Corporation in 2005. Since 2015, he has been a Deputy General Manager of Smart Energy Research Laboratories, NEC Corporation. He has responsibility for the research area of nanotechnology and quantum technology, which include spintronics, nano-phonic devices, quantum information, and printed electronics.



Sadamichi Maekawa was born in Nara Prefecture, Japan, in 1946. He received the B.Sc. and M.Sc. degrees from Osaka University, Osaka, Japan, in 1969 and 1971, respectively, and the D.Sc. degree from Tohoku University, Sendai, Japan, in 1975.

He was a Research Associate from 1971 to 1982, and an Associate Professor from 1982 to 1988 at the Institute for Materials Research, Tohoku University, Sendai, Japan, a Professor in the Faculty of Engineering, Nagoya University,



Nagoya, Japan, from 1988 to 1997, and a Professor at the Institute for Materials Research, Tohoku University from 1997 to 2010. Since 2010, he has been a Director of the Advanced Science Research Center, Japan Atomic Energy Agency, Tokai, Japan. His main research interests include theories of electronic properties in strongly correlated electron systems, in particular, high-temperature superconductors and orbital physics in transition metal oxides, and theories of transport phenomena in magnetic nanostructures.

Dr. Maekawa received Fellow of Institute of Physics (U.K.) in 1999, the Humboldt Award (Germany) in 2001, APS Fellow in 2007, the IUPAP Magnetism Award and Neel Medal in 2012, the Honoris Cause Doctorate of University of Zaragoza (Spain) in 2013, and several Japanese awards.

Eiji Saitoh was born in Tokyo, Japan, in 1971. He received the B.Eng., M.Eng., and Ph.D. degrees from the University of Tokyo, Tokyo, Japan, in 1996, 1998, and 2001, respectively.

He was a Research Associate in the Department of Physics, Keio University, Yokohama, Japan, from 2001 to 2006, and an Assistant Professor in the Department of Applied Physics and Physico-Informatics, Keio University, from 2006 to 2009. He has been a Professor at the Institute for Materials Research, Tohoku University, Sendai, Japan, since 2009, a Professor at the WPI Advanced Institute for Materials Research, Tohoku University, since 2012, and a Visiting Group Leader at the Advance Science Research Center, Japan Atomic Energy Agency, Tokai, Japan, since 2010. Since 2014, he has been a Research Director of the ERATO "Spin Quantum Rectification" project at Japan Science and Technology Agency. He was also a Visiting Scholar at the Cavendish Laboratory, University of Cambridge, Cambridge, U.K., in 2004 and a PRESTO Researcher at the Japan Science and Technology Agency, from 2007 to 2011. He has worked on various fields of condensed matter physics such as strongly correlated electron systems, nanomagnetism, and spintronics. His research is now focused on spin-related phenomena including the generation, detection, and manipulation of spin currents.

Dr. Saitoh received the IUPAP Young Scientist Award in 2009 and many Japanese awards.

